

# JGR Atmospheres

## RESEARCH ARTICLE

10.1029/2019JD031774

### Key Points:

- Mature Oklahoma mesoscale convective systems exhibit more intense, wider convective drafts than Amazon systems
- Drafts intensity increases with core width and with altitude
- Smaller model grid spacing simulations ( $\Delta x < 1$  km) better capture observed draft intensity, width, shape, and mass flux

### Supporting Information:

- Supporting Information S1

### Correspondence to:

D. Wang,  
 diewang@bnl.gov

### Citation:

Wang, D., Giangrande, S. E., Feng, Z., Hardin, J. C., & Prein, A. F. (2020). Updraft and downdraft core size and intensity as revealed by radar wind profilers: MCS observations and idealized model comparisons. *Journal of Geophysical Research: Atmospheres*, 125, e2019JD031774. <https://doi.org/10.1029/2019JD031774>

Received 9 OCT 2019

Accepted 7 MAY 2020

Accepted article online 13 MAY 2020

## Updraft and Downdraft Core Size and Intensity as Revealed by Radar Wind Profilers: MCS Observations and Idealized Model Comparisons

Dié Wang<sup>1</sup> , Scott E. Giangrande<sup>1</sup> , Zhe Feng<sup>2</sup> , Joseph C. Hardin<sup>2</sup> ,  
 and Andreas F. Prein<sup>3</sup> 

<sup>1</sup>Environmental and Climate Sciences Department, Brookhaven National Laboratory, Upton, NY, USA, <sup>2</sup>Pacific Northwest National Laboratory, Richland, WA, USA, <sup>3</sup>National Center for Atmospheric Research, Boulder, CO, USA

**Abstract** This study explores the updraft and downdraft properties of mature stage mesoscale convective systems (MCSs) in terms of draft core width, shape, intensity, and mass flux characteristics. The observations use extended radar wind profiler (RWP) and surveillance radar data sets from the U.S. Department of Energy Atmospheric Radiation Measurement program for midlatitude (Oklahoma, USA) and tropical (Amazon, Brazil) sites. MCS drafts behave qualitatively similar to previous aircraft and RWP cloud summaries. The Oklahoma MCSs indicate larger and more intense convective updraft and downdraft cores, and greater mass flux than Amazon MCS counterparts. However, similar size-intensity relationships and draft vertical profile behaviors are observed for both regions. Additional similarities include weak positive correlations between core intensity and core width (correlation coefficient  $r \sim 0.5$ ) and increases in draft intensity with altitude. A model-observational intercomparison for draft properties (core width, intensity, and mass flux) is also performed to illustrate the potential usefulness of statistical observed draft characterizations. Idealized simulations with the Weather Research and Forecasting model aligned with midlatitude MCS conditions are performed at model grid spacings ( $\Delta x$ ) that range from 4 km to 250 m. It is shown that the simulations performed at  $\Delta x = 250$  m at similar mature MCS lifecycle stages are those that exhibit draft intensity, width, mass flux, and shape parameter performances best matching with observed properties.

## 1. Introduction

Climate predictions of extremes in deep convective cloud (DCC) intensity, such as higher precipitation rates or severe weather potential, point to significant global economic vulnerabilities connected with accurate representations of these clouds in weather and climate models (e.g., Diefenbaugh et al., 2013; Seeley & Romps, 2015; Sillmann et al., 2013; Trapp et al., 2009). The current inadequacies in our observations of the kinematic and/or microphysical characteristics of DCCs inhibit global climate model (GCM) to higher-resolution cloud-resolving model (CRM) process improvement (e.g., Del Genio et al., 2012; Donner et al., 2016; Fan et al., 2017; Mrowiec et al., 2012; Varble et al., 2014). A fundamental property of convection is its vertical air motion, which is one of the most difficult aspects of DCCs to measure by direct observations. Recent CRM studies that attempt to evaluate the simulated convective updraft properties against radar retrievals indicate deficient model representations of updraft magnitudes, frequency, and areal coverage (e.g., Varble et al., 2014; Fan et al., 2017). Since such air motion retrievals are scarce, there is continued motivation to improve the documentation of updraft and downdraft properties for future model process improvement.

The best observations of DCC updrafts, downdrafts, and/or mass flux properties have been historically those collected by aircrafts (e.g., Anderson et al., 2005; Byers & Braham, 1948; Heymsfield et al., 2010; LeMone & Zipser, 1980; Stith et al., 2004; Zipser, 1977; Zipser & LeMone, 1980). Unfortunately, in situ or remote sensing-based aircraft observations of deep convective updrafts are costly, hazardous, and infrequent, having additional maximum aircraft altitude, endurance, and safety restrictions. Recently, profiling and scanning Doppler radar and/or multifrequency remote sensing techniques have also been suggested as partial solution to this absence of vertical air motion information within DCCs (e.g., Giangrande et al., 2016, 2013; Kollias et al., 2018; Kumar et al., 2015; May & Rajopadhyaya, 1996, 1999; North et al., 2017; Ovchinnikov et al., 2019;

Ray et al., 1980; Williams, 2012). The modest spatiotemporal resolution ( $O(1 \text{ km}, <5 \text{ min})$ ), accuracy (often reported within 1–2 m/s in deep convective core regions for “instantaneous”/gate retrievals; e.g., Heymsfield et al., 2010), and availability for multiyear data sets are strengths for these methods. Remote sensing measurements are currently also the best option to inform on intense DCC updrafts considering practical restrictions of severe storms on aircraft operations.

This study is motivated by the need to better document DCC updraft/downdraft properties as can be retrieved using an extended radar wind profiler (RWP) data set. To narrow our observational scope, the analyzed data set is drawn from a mesoscale convective system (MCS) archive recently summarized by Wang et al. (2019). As among the largest and most intense type of convective storms, MCSs are recognized for their important role at local (e.g., severe weather warning) to global (e.g., general circulation and water cycle) scales (e.g., Del Genio & Kovari, 2002; Feng et al., 2016, 2018; Fritsch et al., 1986; Hartmann et al., 1984; Houze, 2004, 2018; Nesbitt et al., 2006; Roca et al., 2014). From a practical perspective, mature MCSs and/or squall lines having trailing stratiform precipitation typically represent one of the more well-defined targets to identify and sample with existing ground-based radar equipment. These data sets were collected by the U.S. Department of Energy’s (DOE) Atmospheric Radiation Measurement (ARM; Mather & Voyles, 2013) program at its field site in Oklahoma, USA, as well as by its Mobile Facility (AMF; Miller et al., 2016) deployment to the central Amazon Basin. Moreover, a secondary benefit for this data set is that it includes RWP observations collected within two archetypal continental MCS locations that potentially allow demonstration for regional (midlatitude and tropical) and seasonal kinematic variability.

An emphasis for this study is on mature MCS updraft and downdraft properties in terms of draft core width, shape, and intensity characteristics. This will include select studies into the variability of those properties with changes in storm regional (midlatitude and tropical) and/or environmental controls. As with the previous RWP-based study by Giangrande et al. (2013), updraft and downdraft characterizations adopt several standard aircraft and profiler-based definitions (and limitations) for draft width, intensity, and mass flux (e.g., LeMone & Zipser, 1980; Zipser & LeMone, 1980). In section 2, we provide information on the data sets and methods to include details on our techniques and sampling considerations when estimating vertical air velocity and core width. Results from these Amazon and Oklahoma MCS data sets that include core size-intensity behaviors and select thermodynamic controls on core properties are presented in section 3. To demonstrate the potential usefulness for extended RWP retrievals, section 4 presents a model-observational intercomparison of convective core properties drawn from idealized MCS event simulations. These simulations are performed using model grid spacings ( $\Delta x$ ) that span  $\Delta x = 4 \text{ km}$  to  $250 \text{ m}$  to better resolve salient storm aspects including large-scale turbulent motions, wind shear, and microphysical processes. Observational and model intercomparison results are further discussed in section 5. A summary of the key findings is presented in section 6.

## 2. Data and Methods

Data sets for this study were collected during continental midlatitude and tropical MCS events recently summarized by Wang et al. (2019). This study focuses on MCSs at a mature lifecycle stage when passing over ARM sites. All events in this data set are characterized as classical leading convective squall-line and trailing stratiform precipitation MCS modes; thus, these MCS events are not intended to be representative of all tropical or midlatitude MCS behaviors (e.g., R. A. Houze, 2004, 2018). Our tropical MCS dataset was collected by the U.S. DOE ARM facility during its ‘Observations and Modeling of the Green Ocean Amazon 2014–2015 campaign, near Manaus, Brazil, from March 2014 to December 2015 (herein, GoAmazon2014/5 or MAO; e.g., Giangrande et al., 2017; Martin et al., 2016, 2017). The midlatitude MCS data set was collected at the ARM Southern Great Plains (SGP) supersite near Lamont, Oklahoma, USA (e.g., North et al., 2017; Sisterson et al., 2016) during the period 2012 to 2016. As summarized in Tables S1 and S2 in the supporting information, the data set includes 42 MCS events from the Amazon campaign that deployed a single RWP at its primary location (i.e., MAO site). The midlatitude MCS data set has 12 events as sampled by four SGP RWPs (one at the SGP Central Facility [CF] in Lamont, OK, and three located at extended facilities within 30 km of the CF). Surveillance weather radar available during each deployment enabled the identification of mature MCS stages, as well as storm tracking capabilities required to estimate core widths as described in section 2.3.

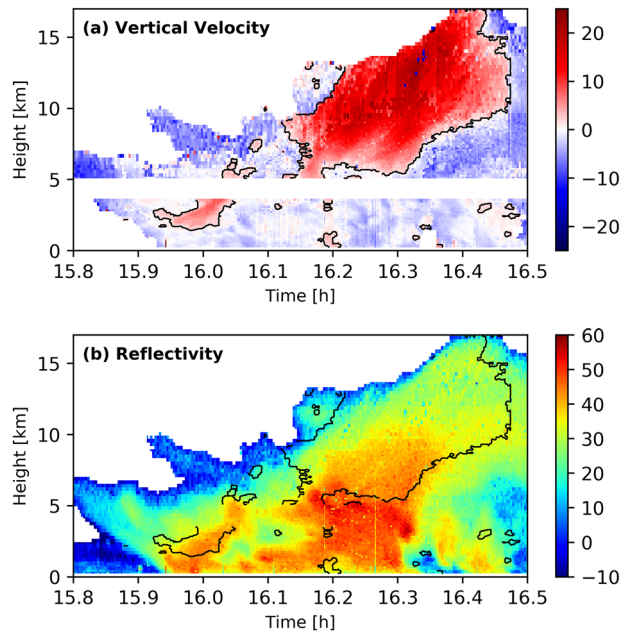


**Figure 1.** Example of RWP (a) retrieved vertical air velocity [m/s] and (b) radar reflectivity factor [dBZ] time-height plots for the 29 March 2015 MCS event during GoAmazon2014/15 field campaign. Contours are the outlines of updraft core regions as designated by our threshold criteria.

## 2.1. ARM Atmospheric Measurements and Event Selection

A suite of surface and sounding instrumentation available at ARM sites and deployments is used in support of this study and event selection. All events required an RWP to sample the convective line and to record an echo top height (ETH) estimate to an altitude that exceeds 12 km. Additional manual checks of the surveillance radar confirmed the presence of a mature stage MCS. Each event in our data set was also required to record an intense rainfall rate ( $R$ ) measurement (as from disdrometer; ARM, 2014) at the time of the convective line passage  $R > 10$  mm/hr. The surface disdrometer measurements in trailing stratiform regions of these MCS events were consulted to minimize RWP reflectivity factor calibration offsets for subsequent velocity retrievals performed in this study (relative accuracy within 1–2 dBZ; e.g., Williams, 2012).

ARM radiosondes (typically launched at 6 hr intervals) provided the thermodynamic quantities of interest for this study (ARM, 2019). Our event selection required the availability of a prestorm radiosonde launched within 4 hr of the convective line and in rain-free conditions. We provide a listing of the events and the radiosonde thermodynamic and convective forcing parameters in Tables S1 and S2, with those parameters estimated using methods found in Wang et al. (2019). These quantities include estimates for the convective available potential energy (CAPE) and the convective inhibition (CIN), as well as 0–5 km Relative Humidity (RH) and 3–6 km Environmental Lapse Rate (ELR). The originating parcels for CAPE and CIN estimates are defined by the level of the maximum vir-

tual temperature in the lowest kilometers. Thus, these quantities represent the most buoyant parcel in the boundary layer and maximize the calculated values such that the reported values are comparable to Most Unstable CAPE/CIN (MUCAPE/MUCIN).

## 2.2. Radar Wind Profiler (RWP) and Vertical Air Velocity Retrievals

The RWPs were the primary instrument for this study and operated at ultrahigh frequency of 920 MHz at SGP (U-band) and 1,290 MHz at MAO (L band). These radars have been reconfigured from standard wind profiling modes to enable unique precipitation sampling that frequently points vertically and collects data through the depth of deep convective cells (to 17 km; e.g., Tridon et al., 2013). The ARM RWPs have a modest beamwidth ( $\sim 9^\circ$ , or 1 km at 6 km AGL;  $\sim 2$  km at 12 km AGL) and observe time-height estimates for the radar reflectivity factor ( $Z$ ) and mean Doppler velocity at approximately 10 s temporal and 200 m gate resolution. Note, RWP  $Z$  values measured below 1.5 km are less reliable for use, owing to RWP receiver saturation (e.g., Tridon et al., 2013). For the 920/1,290 MHz frequencies taking advantage of shorter precipitation mode averaging periods, there are negligible Bragg contributions for the proposed RWP applications in deep convective cores. Measurements collected above 12 km are also not considered for this study, owing to limited RWP samples above these altitudes and additional beamwidth considerations (beamwidths exceed 2 km).

An example of an MCS passage as viewed by the RWP ( $Z$  estimates and retrieved vertical velocity, with overlaid updraft core designation regions as discussed in section 2.4) is plotted in Figure 1 for the 29 March 2015 event during GoAmazon2014/5 campaign (Feng & Giangrande, 2018). Convective core vertical air motion ( $W$ ) estimates follow retrieval methods that apply  $Z$ -based fall speed corrections to the estimated RWP mean Doppler velocity as previously performed by Giangrande et al. (2013, 2016) for Oklahoma and Amazon conditions, respectively. Convective core retrieval techniques also employ a filtering of the RWP data sets by identifying the “convective” RWP columns using standard profiler-based concepts that consider column  $Z$  signatures, mean Doppler velocity, and presence of radar “bright band” (melting-level) characteristics (e.g., Fabry & Zawadzki, 1995; Geerts & Dawei, 2004; Williams et al., 1995). Since such radar echo classifications are not completely robust or continuous in time, we ensure reliable and coherent squall-line/periphery convective region identification through additional manual inspection of each event. We do not perform retrievals for altitudes between 3 and 5 km to avoid potential melting hydrometeor contamination in radar  $Z$  measurements. This step is precautionary and not a requirement for deep convective cores having graupel

and frozen drops; this censoring is necessary in periphery stratiform/dry snow regions where increases in  $Z$  through aggregation and melting processes do not imply faster hydrometeor fall speeds.

As before, we apply the previous Giangrande et al. (2013, 2016) methods to similar ARM RWP measurements. Since RWP mean Doppler velocity measurements reflect the contributions from the ambient air motions and particle fall speeds,  $W$  is estimated by removing hydrometeor fall speed contributions according to power law relationships of the reflectivity factor  $Z$ . For rain below the melting level, these relationships are of the form, fall speed  $V_t$  [m/s] =  $aZ^b$ , wherein  $Z$  is in linear units [ $\text{mm}^6/\text{m}^3$ ] and the coefficients  $a$  and  $b$  are based on local disdrometer measurements (e.g., for convective rain). Our power law relationships follow the forms for Oklahoma and Amazon introduced by Giangrande et al. (2013, 2016), who utilize different  $a$  coefficients ( $a = 2.95$  for SGP;  $a = 2.65$  for MAO) with the same  $b$  coefficient (0.1). These differences are physically consistent with regional convective process and DSD variability expectations between midlatitude and tropical continental settings (e.g., higher propensity for smaller drops for the same  $Z$  in tropical settings, or melting graupel or small hail in the Oklahoma setting). Above the melting layer, we estimate a “rain” and a “graupel” fall speed and apply whichever fall speed is slower for a given  $Z$ . The graupel relationship follows from the previous literature (e.g., Giangrande et al., 2016; Heymsfield et al., 2010). The power law relationships used for graupel at SGP site is

$$V_t = 2.2 + \sqrt{10^{(Z-33)/10}} \quad (1)$$

and

$$V_t = 2.3 + \sqrt{10^{(Z-30)/10}}, \quad (2)$$

at the MAO site ( $V_t$  is in units [m/s], and  $Z$  is in units [dBZ]). Again, the smaller coefficients in the MAO relation are consistent with physical expectations for continental-tropical events associated with higher-density graupel and/or frozen drops when compared to SGP events. Additional discussion on the development, modifications, and intercomparison of graupel fall speed behaviors with dual frequency-based retrievals is found in Giangrande et al. (2013, 2016). Previous studies indicate that RWP retrievals of this form are accurate within 1–2 m/s provided the absence of larger hail. While Amazon events do not promote hail, Oklahoma events were cross-referenced with NOAA’s National Weather Service Storm Prediction Center storm reports to mitigate inclusion of possible large hail events. Comparisons of single profiler concepts in tropical convection to dual-frequency profiler “residual” fall speed behaviors (e.g., Figure 5 as from Giangrande et al., 2016) also indicate previously established model-based power law forms align in a consistent way to independent bulk fall speed  $V_t$ - $Z$  relations, with differences within 1–2 m/s. Note that these statements are “instantaneous” retrieval expectations and subsequent sections will introduce that for the relevant “core” properties (e.g., the maximum updraft in a given core); random sampling and other factors promote additional biases that are scale independent and may exceed 30–40% for any given core.

### 2.3. Surveillance Radar-Based Tracking

A nearby surveillance S-band (3 GHz) radar was available within 70 km of each site and used to estimate horizontal advection speed of the MCS propagating over the RWPs (e.g., Figure 2). At the SGP site, the Next-Generation Radar (NEXRAD) provided radar coverage over the CF and intermediate RWP locations. Surveillance radar coverage during GoAmazon2014/5 over the ARM site was obtained from the closest System for the Protection of Amazonia (SIPAM) S-band radar located near Manaus (e.g., Martin et al., 2016). Radar fields were quality controlled for clutter and then transformed to a Cartesian grid. The Vance AFB NEXRAD (KVNK) radar data were gridded to a 1 km  $\times$  1 km horizontal grid and available at approximately 5 min intervals. The SIPAM radar data were gridded to a 2 km  $\times$  2 km horizontal grid and available every 12 min.

For all MCSs passing over the sites, radar data were used to estimate advection speed of the convective features associated with the MCSs using the FLEXible object TRAcKeR (FLEXTRKR) tracking algorithm in Feng et al. (2018). First, radar data were processed to classify the approximate convective and stratiform areas by applying a tuned version of the Steiner et al. (1995) classification technique (Feng et al., 2012) to the radar reflectivity field at 2.5 km MSL. Convective features are defined as contiguous grid points classified as “convective” and are tracked temporally based on the overlap. This provided a series of 2-D reflectivity images for the same convective features. Once the tracked 2-D reflectivity images have been generated,



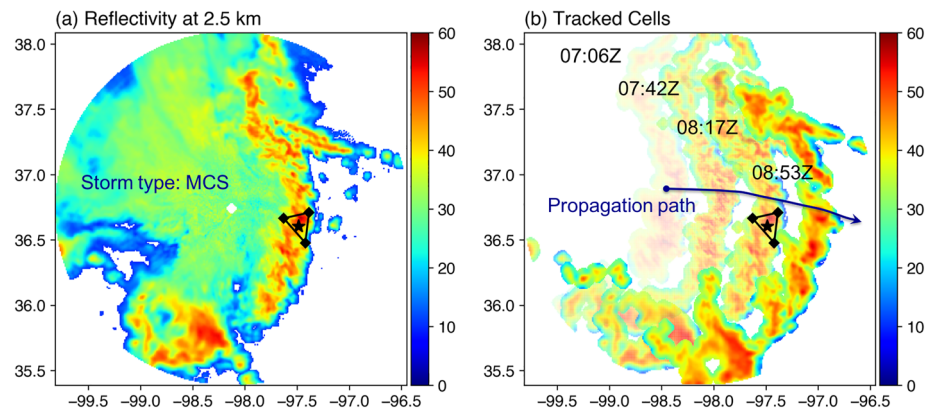


**Figure 2.** Example of radar tracking for the 5 June, 2013 MCS event over the SGP site from the KVN X NEXRAD radar. (a) Snapshot of CAPPI radar reflectivity at 2.5 km MSL, (b) representative snapshots of the tracked MCS convective feature at several different times as it propagated eastward over the SGP site. The star represents the SGP CF, and the three diamonds forming a triangle denote the three extended facility sites surrounding the CF.

storm advection is calculated as the 2-D spatial shift that maximizes the cross-correlation between two-time steps. The use of the cross-correlation technique avoids unrealistic jumps in tracking performance caused by changes in MCS morphology. Using the calculated advection and time lag, convective storm propagation speeds were estimated. In cases where the 2-D correlation fails to find a realistic advection rate for a time step ( $<50$  m/s), the result is interpolated using a spline fit from the time series of advection speed for the tracked feature. Results of MCS tracking are listed in Tables S1 and S2.

#### 2.4. Updraft/Downdraft Core and Core Mass Flux Definitions

Previous aircraft studies have defined cores as contiguous regions where an aircraft samples vertical air velocity  $|W|$  exceeding 1 m/s for a minimum of 0.5 to 1 km distance (e.g., LeMone & Zipser, 1980). For time-height profiler studies as in May and Rajopadhyaya (1999) or Giangrande et al. (2013), their core designations have adopted a more restrictive air velocity threshold  $|W| > 1.5$  m/s to accommodate additional retrieval RWP uncertainty, as well as identifying velocity features having a 1 min contiguous measurement that exceeds this velocity threshold. The justification for the 1 min standard was that for modest convective storm propagation speed (15 m/s), a 1 min sample translated to the approximate capture of a 1 km core. In this study, we adopt the same approach as in previous profiling radar efforts recognizing the “trial-and-error” and/or arbitrary nature for both aircraft and profiler core thresholds as noted by those previous authors. Overall, this 1 km benchmark is a rough guideline for a minimum allowable or trustworthy core. However, larger/smaller core designations may be anticipated under faster/slower storm propagation speeds, or when sampled at different altitudes (e.g., eventual beamwidth limitations to higher altitudes).

RWP sampling was performed using an approximate 14 s update cycle, interweaving precipitation sampling (7 s) and boundary layer wind sampling (7 s). The precipitation mode data have been linearly interpolated to 10 s. Thus, our proposed core designations require six or more contiguous observations from the RWPs that exceed our minimum velocity threshold. As in Giangrande et al. (2013), additional criteria are used to reduce spurious or less significant designations. Criteria include applying a vertical core continuity check, as well as thresholds for significant mean core reflectivity factor ( $\langle Z \rangle > 20$  dBZ). We maintain an upper bound of 12 km when we plot 1-D histograms and 2-D core size relationship, which aligns our comparisons to those from the previous (Giangrande et al., 2013) study. Note that this plotting choice is also a practical reflection of the limited core samples above those heights (fewer than 100 cores sampled above 12 km). This is attributed to a decreasing number of storm sampling opportunities (fewer cloud columns that reach higher altitudes), as well as RWP beamwidths that exceed 2 km, thereby less enabling smaller core properties to be sampled. Additional RWP core sampling “trial-and-error”-type considerations are discussed in section 2.5.

Air mass flux calculations follow constant-altitude aircraft definitions as in LeMone and Zipser (1980). These estimates represent the rate of transport of mass per unit distance perpendicular to the profiler time/diameter dimension. The mass flux values are determined by an expression ( $\rho WD$ ) that is the product of the air density  $\rho$ , the mean/median air motion  $W$ , and core width (or approximate diameter)  $D$ . This definition, much like core mean or core maximum air velocity values, is a property of an individual core. Thus,

these mass flux estimates are different than a traditional GCM-type definition for mass flux in cumulus parameterization that requires estimating the properties of all cores over a large area (e.g., found in recent RWP studies in Giangrande et al., 2016; Kumar et al., 2015). The core width  $D$  is calculated using the mean convective line propagating speed for each individual MCS event, multiplied by the number of continuous time bins (at 10 s spacing).

### 2.5. Additional Core Sampling, Plotting, and Designation Considerations

Profiler studies are typically presented in a similar fashion to previous aircraft core studies, as these methods share several advantages and limitations. Profiler methods assume that the width of convective drafts sampled steady state (in time height) and do not evolve substantially during the collection window. In addition, RWP efforts assume that storm propagation is similar to collective convective draft propagation. These potential discrepancies may be partially offset by RWP capabilities to inform or filter on the coherent (2-D) nature of the sampled drafts (e.g., vertical continuity and associated checks). Nevertheless, RWP retrievals share in several sampling and interpretation considerations as previously discussed by aircraft studies (e.g., LeMone & Zipser, 1980). This section summarizes these shared considerations for the current RWP applications.

Both aircraft and RWP sampling are forms of random core sampling, wherein the sampled core properties may not reflect direct hits over the RWP site. One solution for such associated “random” sampling biases has been provided by Jorgensen et al. (1985), associated with a generalized random-radius sampling of circular core objects. This particular solution to the random core sampling problem is scale independent and follows RWP retrieval assumptions to include MCS squall lines containing randomly placed circular drafts propagating over the profilers in a consistent manner. For these circular drafts, an expectation diameter (chord) would be biased low by approximately 22% (see mathematical derivations in Jorgensen et al., 1985). The current RWP retrieval methods remove smaller objects/chords of  $O(0.5 \text{ km})$ , and this acts to reduce the expectation diameter biases in a scale-dependent manner. However, applying this scale-dependent change to the Jorgensen et al. (1985) solution is of minimal impact (e.g., within 5%) for cores larger than 1 km, asymptotes to the approximate 21–22% underestimate (statistically) for core diameters larger than 2 km. Owing to nonuniform beam filling considerations, 2 km and larger cores considered in this study will have core widths smeared by as much as half the beam width (e.g., 500 m at 6 km). In these practical RWP applications, smearing will mitigate expected underestimation to higher altitudes, but typically not to better than 10–15% underestimation for the larger cores.

Jorgensen et al. (1985) further discussed the impact of this random sampling on core velocity properties when assuming drafts behaving as triangular (e.g., cores having a peak velocity in the center and linear decrease in velocity to core edges). In this configuration, the expected maximum velocity  $W_{max}$  would be underestimated by a factor of 2. With regard to this statement on  $W_{max}$  (or  $< W >$ ) sampling bias, it is known the limiting assumption to establish these sampling biases is that of triangular core behaviors, given that a flatter/“top hat” draft shape would promote reduced to no biases. In observation results from section 3, we suggest the triangular draft assumption is reasonable from our RWP records and therefore the MCS draft intensity properties we report are potentially biased low by a factor of 2. Testing performed on modeled MCS cores to higher grid spacing (simulations introduced in section 4) indicates that applying similar random core sampling ideas to model outputs consistently promotes diameter biases to the 20% level. However, our model runs indicate  $W_{max}$  from our core sampling method is biased low by approximately 30–40% (not shown), with higher underestimation to larger core sizes. Here, we attribute this discrepancy when using models for expected  $< W >$  or  $W_{max}$  bias to model simulated updraft shape that is more “top hat” like than triangular like, possibly owing to wider drafts (or higher resolution) better resolving more triangular (see discussions in section 5).

For 2-D size-intensity relationships we provide in subsequent sections, chording considerations also imply that sorted core width behaviors are potentially informed by a population of chords that originate from wider cores. As wider cores are typically more intense, it is suggested that select biases in 2-D plotting representations may be introduced (e.g., sampling wider cores as if these were smaller), offset partially (especially for triangular-type features) by the corresponding increase in core magnitude. Biases in these averaged core properties attributed to chords from significantly larger cores are however mitigated by the overall decrease in core counts to extreme sizes.

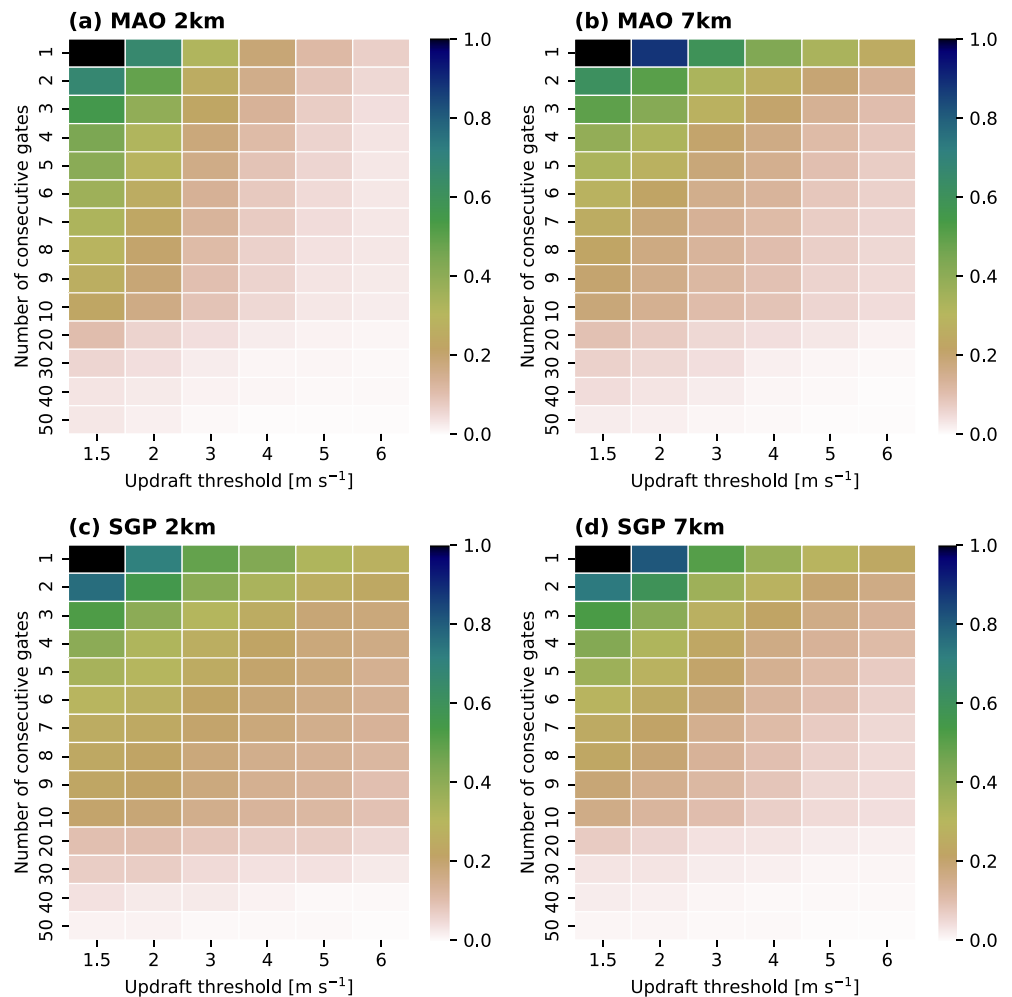


**Figure 3.** Normalized number of updraft cores at 2 and 7 km as a function of vertical velocity threshold and the number of consecutive gates used for defining the convective cores, for MAO (a and b) and SGP (c and d) MCSs.

Finally, it is expected that changes to our core threshold criteria (velocity or consecutive/coherent observations) will impact our designation of weaker and/or smaller-sized features. Ideally, we do not want small changes in method thresholds to cause significant changes to our summary core results (e.g., for cores larger than 2 km). In Figure 3, we plot 2-D histograms for the normalized number of updraft cores sampled for the SGP and MAO MCSs at two altitudes (2 and 7 km). In this plot, we display the sensitivity of updraft core counts to a range of minimum core velocity and minimum core size (consecutive RWP time sample) criteria. As expected, applying higher-velocity threshold criterion (allowing only core objects greater than 1.5 m/s) reduces the number of cores by removing less significant features. However, the change in updraft core count is relatively insensitive to small increases in the velocity threshold. Thus, we suggest it is appropriate to maintain the  $W$  threshold of 1.5 m/s, as the value aligns with several previous studies. The more significant change to core counts is associated with the requirements for contiguous observations when identifying a core. Here, our testing indicates a rapid increase in counts when attempting to designate cores without ensuring there are five to six consecutive time gates reporting this core. This inflection point is aligned with previous six-gate/1 km criteria as adopted by RWP efforts and attributed to additional RWP beamwidth considerations, for example, less able to resolve core objects smaller than 1 km under high altitude or fast-moving MCS conditions.

### 3. Core Results Within Mature MCS Convective Lines

Kinematic characteristics observed during mature stage MCS updraft and downdraft cores are summarized in this section. Although we limit our examples to the mature stages in the MCS lifecycle, any

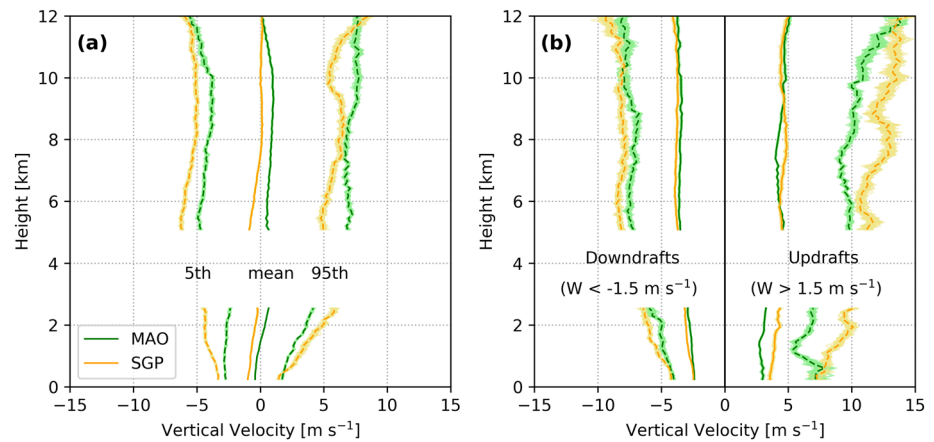


**Figure 4.** (a) Mean (solid line), 5th and 95th (dashed lines) vertical velocity profiles for SGP and MAO MCS events within convective region. (b) Vertical velocity profiles for SGP and MAO MCS convective downdrafts ( $W < -1.5 \text{ m s}^{-1}$ ; left side) and updrafts ( $W > 1.5 \text{ m s}^{-1}$ ; right side). The shading is the spread from random sampling of half of the data set (100 times).

lifecycle assessment based on the presence of key radar squall-line precipitation properties is nonetheless nontrivial to generalize. Moreover, we anticipate that mature MCS transition from updraft-dominant to downdraft-dominant phases, for example, as reflected by changes in mature-stage convective and stratiform precipitation coverage (e.g., Feng et al., 2019). Thus, the authors recommend caution when interpreting the mature-stage results that follow.

In Figure 4, we introduce the MAO and SGP data sets by plotting the cumulative mean, 5th (downdraft) and 95th (updraft) percentile profiles for the vertical air motion ( $|W| > 1.5 \text{ m/s}$ ) in convective regions. These composites are similar to the ones found in Wang et al. (2019) and other observational summaries. In Figure 4b,

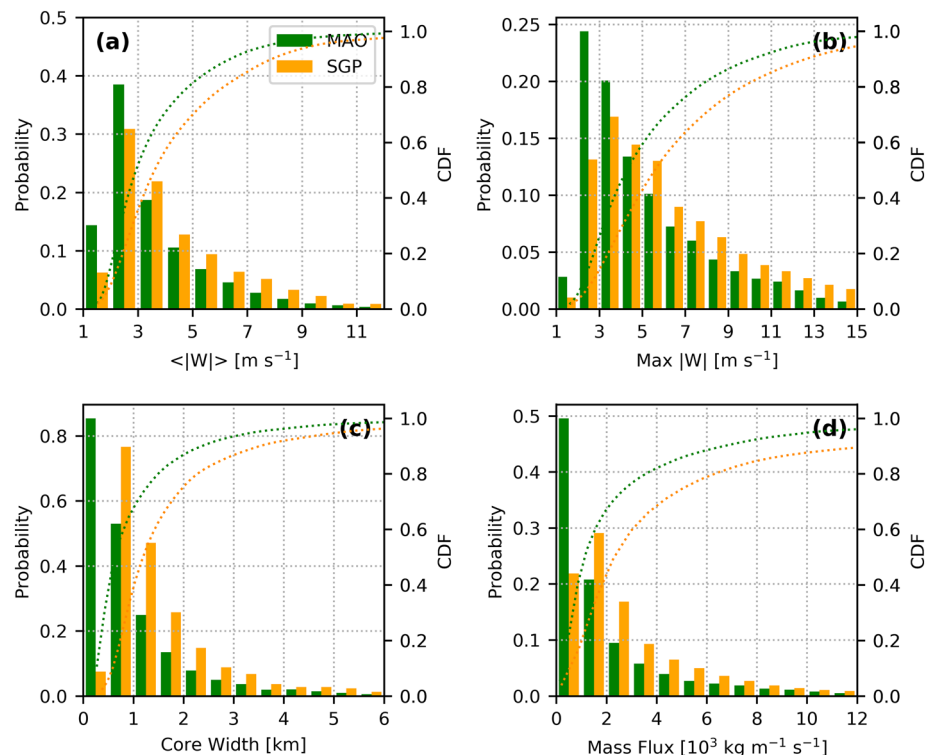


**Figure 5.** Histograms and cumulative distribution functions (CDFs, dotted lines) of updraft cores mean vertical velocity (a), maximum vertical velocity (b), core width (c), and mass flux (d) for MAO and SGP MCSs.



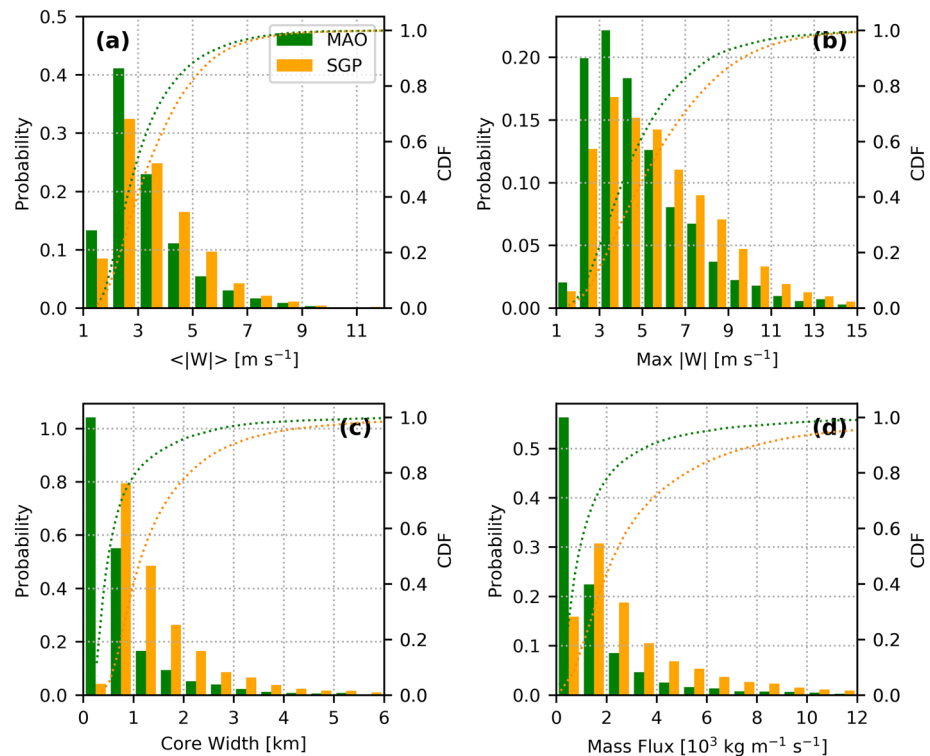


**Figure 6.** As in Figure 5 but for downdraft cores.

we demonstrate that when segregating according to updraft-only ( $W > 1.5$  m/s) and downdraft-only ( $W < -1.5$  m/s) conditions, SGP events are associated with more intense air motions. Both MAO and SGP MCSs indicate extreme (5th and 95th percentiles) air motions exceeding 10 m/s. Profile mean and tail-end values indicate that more intense air motions are observed at higher altitudes.

### 3.1. Updraft and Downdraft Core Histograms

Core width, mean, maximum vertical velocity, and mass flux are computed as in Giangrande et al. (2013). For the SGP data set, approximately 7,972 updraft cores and 10,493 downdraft cores were designated using the six-gate/1.5 m/s threshold criteria. For the MAO data set, core counts are 14,952 and 8,951 for updrafts and downdrafts, respectively. Overall, core counts in this data set are a factor of 3 larger than the data sets summarized by the Giangrande et al. (2013) study.

In Figures 5 and 6, we plot 1-D normalized histograms and cumulative distribution functions (CDFs) for updraft and downdraft cores. Since midlatitude SGP events are typically associated with larger-scale forcing (e.g., frontal Feng et al., 2019; Song et al., 2019) and steeper ELRs, especially during spring time (Tables S1 and S2), these events promote more intense in-cloud motions (Figures 5a and 5b). For example, approximately 20% of the SGP data set registers a maximum updraft velocity  $>10$  m/s, as compared to 10% of the MAO data set cores (e.g., Figure 5b). Wide updraft cores ( $D > 6$  km) are not frequently observed at either location (e.g., Figure 5c). Since SGP updrafts are more intense and more frequently wider, SGP core distributions skew toward a higher mass flux. Downdraft core distributions (Figure 6) align with updraft results, suggesting wider cores (Figure 6c) and more intense downdrafts (Figures 6a and 6b) for SGP. Downdrafts are weaker than updrafts, with core widths smaller than those for updrafts (predominantly,  $D < 4$  km). Recall that these downdrafts are exclusively sampled in the convective regions, not those observed in the stratiform portions of the MCSs.

### 3.2. Cumulative Core Properties and Dependence With Core Width

One approach to isolate core properties is to sort updraft or downdraft retrievals according to core width. In Figure 7 (updrafts) and Figure 8 (downdrafts), we plot the mean and standard deviations (in 1 km core width increments) for the mean horizontal draft velocity  $\langle W \rangle$ , the maximum velocity  $W_{max}$ , the ratio of the mean horizontal core velocity to its maximum velocity  $\langle W \rangle / W_{max}$ , and mass flux. These figures overlay linear

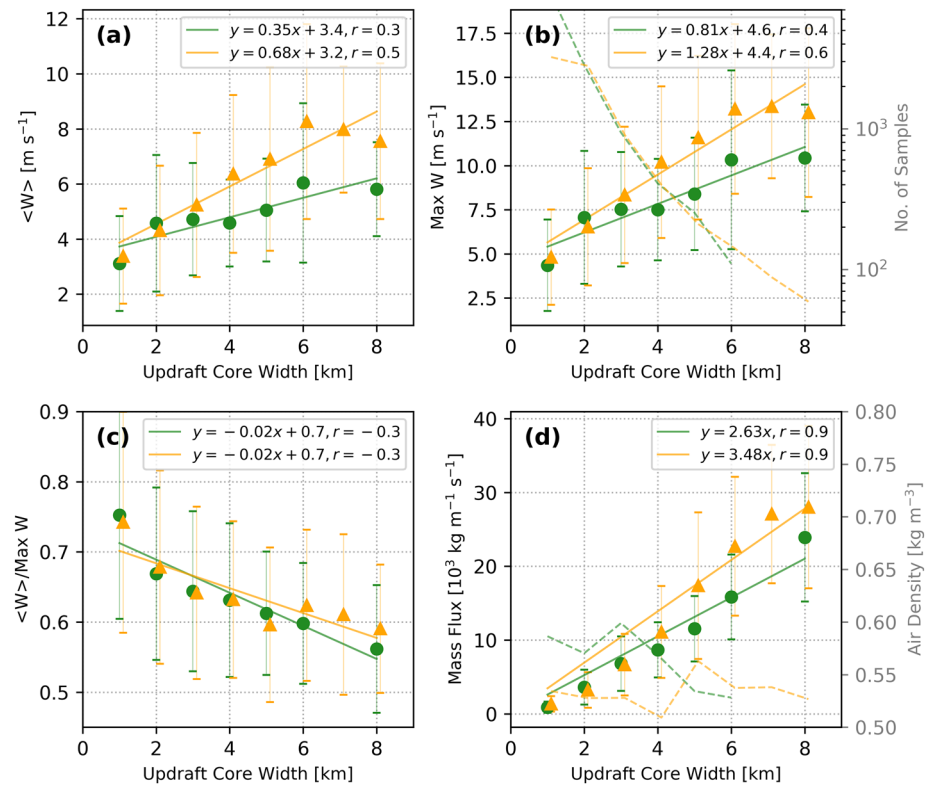


**Figure 7.** Mean vertical velocity (a), maximum vertical velocity (b), mean vertical velocity normalized by the maximum vertical velocity (c), and mass flux (d) for each updraft core width bin at MAO (green) and SGP (yellow) sites (dots). Bins are an increment of 1 km, and error bars represent  $\pm 1$  standard deviation. Solid lines are the linear least squares regression fits.

least squares regression fits to the data sets and the associated Pearson correlation coefficients ( $r$ ) for those relationships (calculated using the whole data set). Correlation coefficients are provided following previous aircraft and profiler studies. However, as correlation coefficients are intended for quantities that are linearly related, these calculations may not be applicable to updraft size and intensity characteristics that involve complex relationships with entrainment and other processes. In Figures 7b and 8b, we report the number of samples within each bin, with fits performed using bins having counts  $> 50$ . In Figures 7d and 8d, we plot the mean air density  $\rho$  associated with the core populations (bin), as reference to the role of  $\rho$  in mass flux estimates. These values serve as a proxy for the average altitude of these core samples.

As reported by Zipser and LeMone (1980) for GARP (Global Atmospheric Research Program) Atlantic Tropical Experiment (GATE) and also by Giangrande et al. (2013) for Oklahoma, we observe a modest increase in mean and maximum updraft intensity as a function of core width ( $r \sim 0.5$ ). The correlation is of similar magnitude to Giangrande et al. (2013), and this weak positive correlation is observed at both sites. There is also a slightly stronger correlation coefficient in core size intensity between the core width and its maximum updraft velocity (than to mean core velocity). Overall, SGP updraft core intensity and mass flux retrievals are more intense at the larger core sizes than MAO counterparts (e.g., larger slope parameters). Note that the average air density in similar size bins (e.g., Figure 7d) also shifts between the SGP and MAO data sets, with the SGP site reporting a lower average air density for cores smaller than 4 km. Moreover, the SGP data sets indicate that the typical updraft core (any size) is sampled to higher altitudes (lower average density across all core sizes), whereas MAO suggests smaller cores dominate the MAO statistics at the lower altitudes (also see Figure S2).

Additional tests (not shown) indicate that the normalized, statistical horizontal core shape is approximately triangular (e.g., symmetric, with  $W_{max}$  located in the center), in agreement with previous suggestions by Zipser and LeMone (1980). We include plots for the ratio  $\langle W \rangle / W_{max}$  (e.g., Figures 7c and 8c) that one may

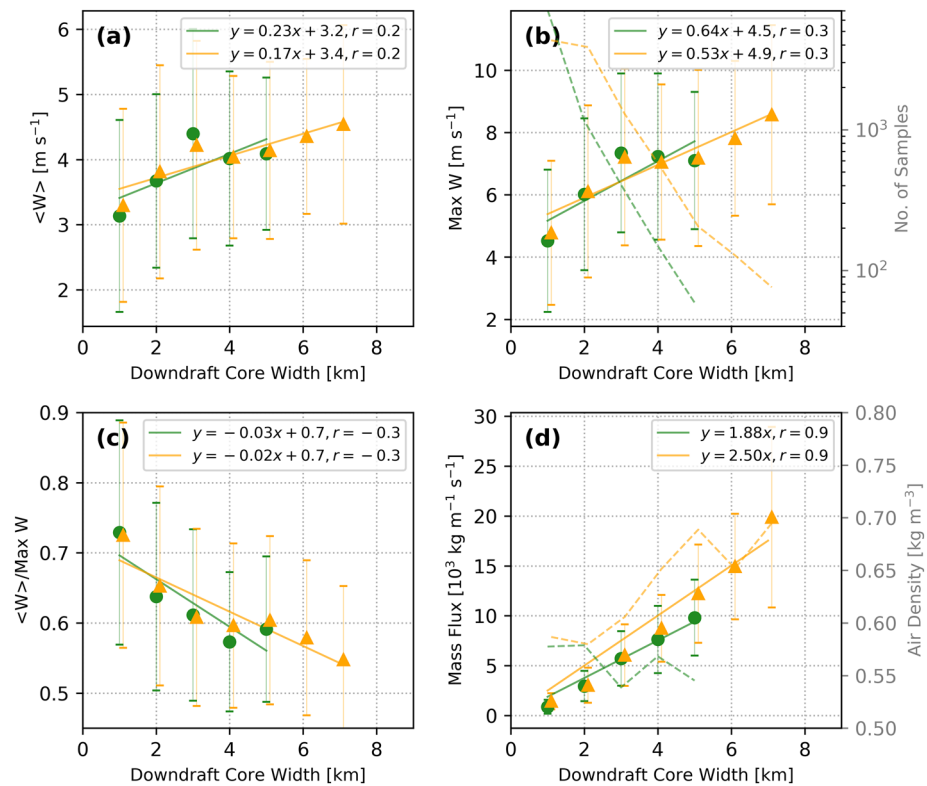


**Figure 8.** As in Figure 7 but for downdraft cores.

interpret as a core shape or peakedness parameter for a triangular core. A similar ratio or assumption (typically, a value of 0.5) is often found in convective cloud models and theoretical treatments such as those in Kuo and Raymond (1980) and Morrison (2016). We find a mean ratio of 0.6 that is similar at both locations. Although the aforementioned studies often assume this ratio as a constant with core altitude/size, our observations indicate a weak, negative correlation for this ratio with size ( $r \sim -0.3$ , Figure 7c; wider drafts appearing more triangular when size can be better resolved by the RWP). Here, discrepancies with the theoretical literature may relate to the RWP's inability to properly capture ratios for the smallest core sizes, but it is encouraging that values closer to 0.5–0.6 are consistent with previous theoretical use.

Owing to its estimation as  $\rho WD$ , we observe a high correlation ( $r \sim 0.9$ ) between the core width and mass flux. The SGP data set favors higher mass flux for the same core width when we compare to MAO owing to these stronger cores (Figure 7d). Mean SGP updraft mass flux values are lower than those reported for Oklahoma by (their Figure 10; Giangrande et al., 2013). For example, the mean mass flux for a 4 km updraft core was reported as  $25 \times 10^3$  kg/s/m, as compared to  $10$ – $15 \times 10^3$  kg/s/m in the current study. Possible factors related to these differences will be discussed in section 5.

In contrast to Zipser and LeMone (1980) aircraft findings, downdraft velocity is positively correlated with core width (e.g., Figures 8a and 8b). These results are consistent with statements from Giangrande et al. (2013), who also reported weak positive correlations for downdrafts using RWP measurements. Overall, there are fewer discernible differences in 2-D downdraft core properties between MAO and SGP data sets as a function of the given draft width. Similar to updraft cores, the ratio  $\langle W \rangle / W_{\max}$  for downdraft cores is approximately 0.6, with a similar weak and negative correlation ( $r \sim -0.3$ ) with increasing size. SGP downdrafts are suggestive of a higher downward mass flux for a given core width (Figure 8d). Although 2-D downdraft properties (e.g., Figures 8a and 8c) indicate SGP downdrafts as similar to MAO counterparts for a given core width, recall that 1-D properties and other attributes are different. Thus, 2-D results still need to be placed in the context of the higher frequency for observing downdraft observations to lower altitudes at SGP when compared to MAO (e.g., Wang et al., 2019).

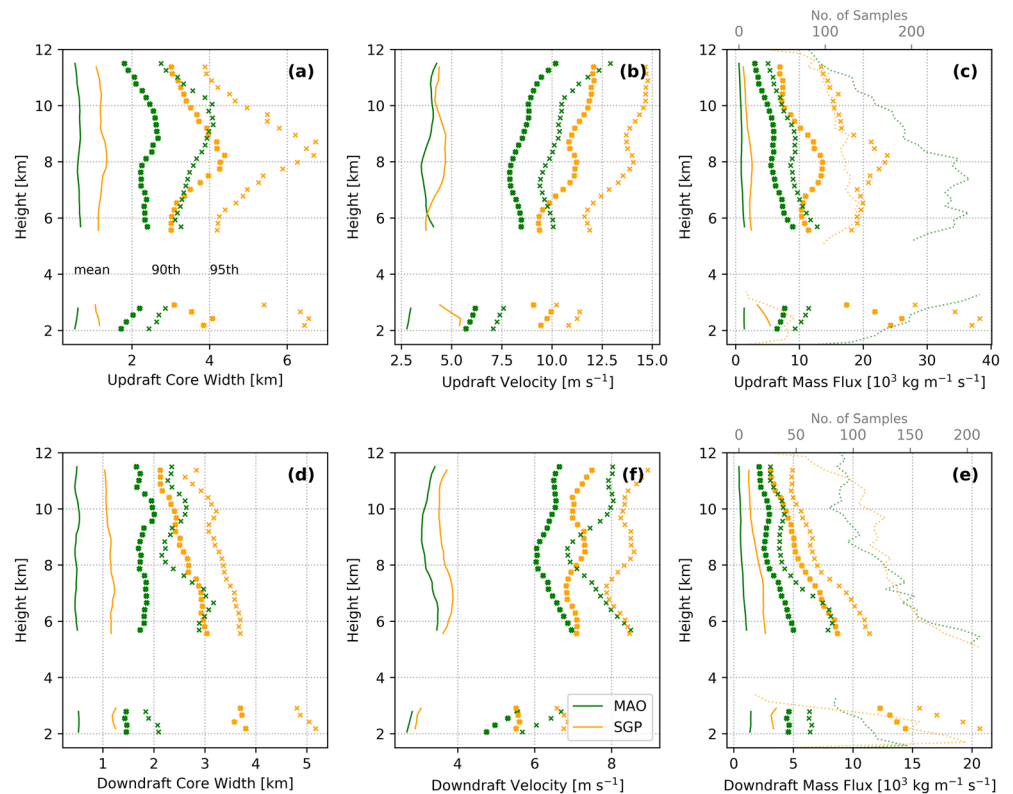


**Figure 9.** Profile statistics of (a) updraft core width, (b) updraft velocity, and (c) mass flux according to the mean, 90th percentile, and 95th percentile. Panels (d) through (f) are for downdraft core properties. The dotted lines are the number of samples.

### 3.3. Velocity, Width, and Mass Flux Profiling

Observational DCC studies often report increases in core vertical air velocity as a function of altitude, with inconclusive statements on the changes in draft width. With respect to mass flux, an increase in updraft magnitude with increasing altitude coupled with the relatively higher frequency of updraft observations (e.g., area fraction) at the midlevels typically suggests a bow-like mass flux profile. In Figure 9, we plot traditional updraft and downdraft core velocity, core width, and mass flux retrieval profiles as a function of altitude. We overlay the 90th and 95th percentiles for these core quantities on each plot. These depictions suggest the following draft characteristics: (a) air motions retrieved in our MCS cores increase with altitude; (b) extremes in updraft and downdraft air motions exceed 10 m/s at higher altitudes; (c) downdraft core width slightly increases toward the surface, with slightly increasing updraft core sizes to higher altitudes; and (d) downdraft mass flux increases toward the surface. Note for these mean and extreme air motion profiles within coherent cores are similar to the ones obtained when applying the simpler  $|W| > 1.5$  m/s definition (Figure 4).

### 3.4. Breakdowns According to Environmental Forcing: MAO Updraft Examples

Giangrande et al. (2016) suggest that different Amazon regimes (e.g., wet or dry season) and/or associated changes in thermodynamic controls (as communicated by CAPE, CIN, or low-level RH) may promote shifts in storm updraft intensity, area fraction, and mass flux profiles as retrieved by RWP observations. Those statements were based on differences between normalized histograms of the vertical velocity retrievals under various regime breakdowns that sampled a wide variety of isolated to organized convective events. For these particular Amazon MCS events, Wang et al. (2019) suggested that Amazon dry or transitional seasons favored more intense maximum updraft profile signatures (distribution tails), with the dry season favoring deeper and more intense downdrafts. However, Wang et al. (2019) were careful to indicate those results as noisy and/or limited by event sampling.

In Figure 10, we reprise updraft characteristics as in Figures 7 and 9 for MCS core properties, as segregated according to Amazon wet (21 events), dry (10 events), and transitional (11 events) seasons. The wet season



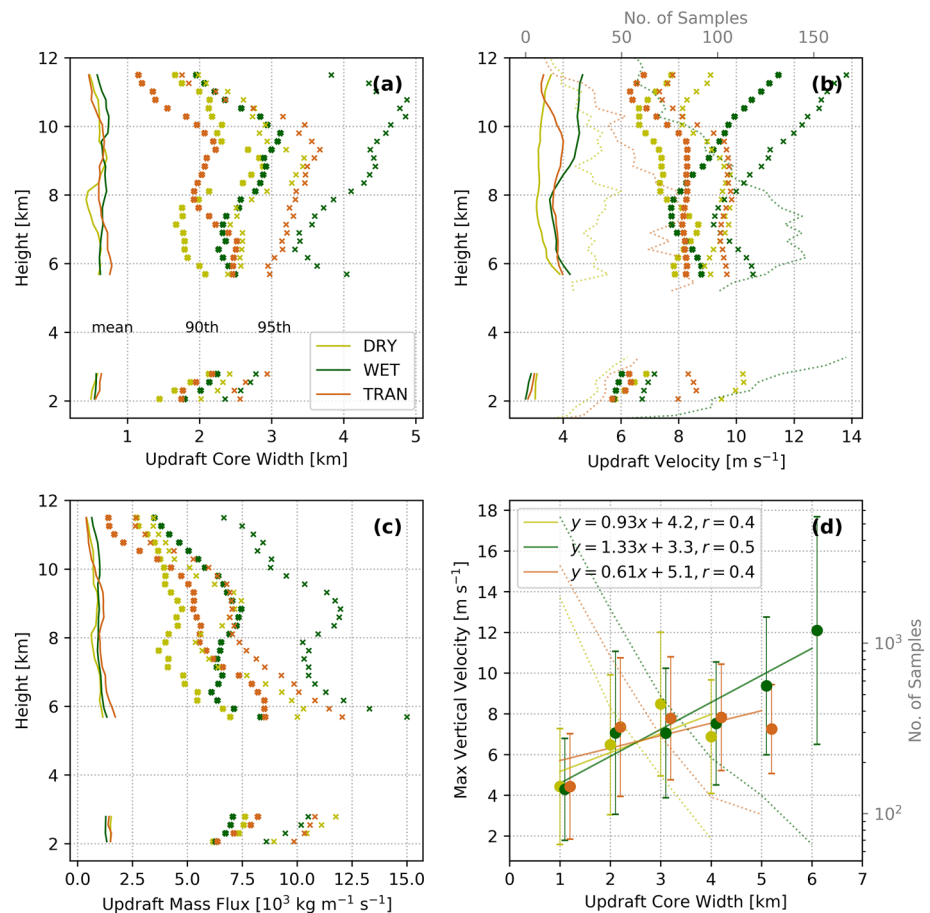


**Figure 10.** As in previous composites, Amazon MCS events segregated according to wet (24 events, dark green), dry (10 events, yellow), and transition (11 events, brown) seasons. The dotted lines are the number of samples.

is defined as MCSs collected between December and April, whereas dry season is defined as events collected between June and September. As summarized in Table S1, the wet and dry season events typically exhibited similar mean CAPE ( $\sim 2,600$  J/kg), CIN ( $\sim -20$  J/kg), and 3–6 km ELR ( $\sim 5.3^\circ\text{C}/\text{km}$ ), but with large interseason variability. Transitional events (those collected during May, October, and November) exhibited higher mean CAPE ( $\sim 3,300$  J/kg) and CIN ( $\sim -30$  J/kg), and similar 3–6 km ELR. For core observations, MCS events do not indicate a significant seasonal shift in updraft intensity (e.g., Figure 10b). However, downdrafts are found to be stronger at higher altitudes in the dry season and/or seasonal conditions having higher CIN (not shown). This may suggest that drier midtroposphere conditions during the dry season (Giangrande et al., 2017) are contributing to stronger downdrafts through raindrop evaporation (dry air is mixed down to the lower levels).

Overall, the absence of a pronounced change in updraft properties is consistent with the lack of variability in MCS thermodynamic conditions across the different Amazon seasons. However, wet season events potentially suggest wider updraft cores at higher altitudes (e.g., Figure 10a) that may accompany enhanced mass flux profile behaviors (Figure 10c). This is consistent with aforementioned Amazon studies that indicate higher wet season upward mass flux owing to larger updrafts/convective area fraction, rather than more intense updrafts.

#### 4. A Comparison of Observed Core Properties to Idealized MCS Simulations

Recent CRM studies report that deep convective simulations favor excessively strong updrafts and incorrect updraft frequency with altitude when evaluating model performance against radar observations (e.g., Donner et al., 2016; Fan et al., 2017; Varble et al., 2014; Wu et al., 2009). Although model performance is often criticized as deficient, a partial explanation for these differences may be attributed to uncertainties in

the radar retrieval methodologies and comparison approaches commonly used in such model-observational evaluations (e.g., Oue et al., 2019). Nevertheless, a likely limitation of previous studies is the use of model grid scales that may not resolve important convective core features, for example, those requiring resolutions to  $O(250\text{ m})$  or less where convective processes are better resolved (including turbulence, entrainment, wind shear, and other factors; Bryan et al., 2003; Bryan & Morrison, 2012; Lebo & Morrison, 2015). The RWP statistics we present in previous sections are capable to resolve cores to  $O(1\text{--}2\text{ km})$ , which may enable  $O(250\text{--}500\text{ m})$  grid spacing model core comparisons (e.g., Skamarock, 2004) to idealized MCS simulations to further these discussions on existing model capabilities.

#### 4.1. Simulated WRF MCSs Event Design and Core Designations

Five MCSs cases are simulated with the Weather Research and Forecasting Model Version 3.9.1.1 (WRF; Powers et al., 2017). WRF is compiled in its idealized configuration, and simulations are performed in a square domain with 620 km side length and 95 vertical levels with equal spacing of 250 m. Rayleigh damping is applied to the top 5 km of the model domain. The domain boundaries are assumed to be open. The main model setups are Thompson microphysics (Thompson et al., 2008) and the YSU planetary boundary layer scheme (Hu et al., 2013). No deep convection scheme is used, since we assume that deep convection is explicitly represented in the model. We neglect the effects of Coriolis acceleration, radiation, and surface fluxes, but we use the Eta surface layer scheme (Janjic, 2002), which helps to form coherent cold pools. To understand the sensitivity of simulated core properties to the model grid size  $\Delta x$ , we performed simulations with  $\Delta x = 4\text{ km}, 2\text{ km}, 1\text{ km}, 500\text{ m},$  and  $250\text{ m}$  without changing any additional model parameters except the model time step.

To initiate convection, we force vertical velocity during the first hour of the simulations within a half cylinder of length 40 km, radius of 20 km, and a depth of 4 km in the vertical similar to Ziegler et al. (2010). The flat side of the half cylinder is located at the surface, and the maximum acceleration of  $2\text{ m/s}^2$  occurs uniformly along the center of the half cylinder, which decays radially as a cosine function of the radius. Random noise helps to trigger 3-D motion and is applied as a potential temperature perturbation with a 0.1 K magnitude in rectangular prisms of  $110 \times 80 \times 4\text{ km}$  size (centered at the location of the half cylinder). The five simulations are initialized with thermodynamic soundings from severe MCS inflow environments that were simulated in a 4 km WRF simulation that downscales ERA-Interim reanalysis data (Dee et al., 2011) over most of North America for the period 2001–2013 (Liu et al., 2017; Prein et al., 2017). These model initial soundings (details as summarized in Table S3) are comparable to the observed prestorm conditions for Amazon and Oklahoma MCSs (see Tables S1 and S2), having wind shear typical of the midlatitudes and mean CAPE ( $2,246\text{ J/kg}$ ) and ELR ( $6.5^\circ\text{C/km}$ ) values that reside in between composite “skinnier” MAO and “fatter” SGP CAPE conditions (e.g., Lucas et al., 1994b, 1994a).

While these idealized soundings are anticipated to better align with midlatitude SGP conditions, these do not reflect archetypal SGP MCS radiosonde conditions. For example, the soundings feature relatively higher 0–5 km RH (90%) and reduced CIN ( $-22.4\text{ J/kg}$ ) conditions than is typical for either the SGP or MAO conditions (Table S3). Note that a higher 0–5 km RH may promote weaker downdraft intensity or structures less typical of the SGP events (e.g., see discussions in Wang et al., 2019). Similarly, higher RH conditions are also associated with wider and intense updrafts in simulations (Morrison, 2017). The simulation runtime is 7 hr, and model outputs are stored in 5 min intervals. We analyze the final 3 hr of the simulations, which corresponds to the mature MCS phases as based on visual inspection.

For comparisons with RWP observations, 5 min WRF output intervals are too coarse to derive perfectly aligned 2-D time-height core statistics. For these initial efforts, instantaneous 3-D model outputs are used to estimate core properties following a similar criterion for draft and mass flux definitions (as described in section 2) as allowable from 5 min outputs. These selected criteria include identifying features having  $|W| > 1.5\text{ m/s}$ , deeper (vertically) than 500 m (to ensure vertical continuity), and wider (horizontally) than 1 km. These cores are collected from randomly drawn 2-D slices through the simulated convective lines. Simulated cores also require a minimum mean reflectivity factor ( $Z > 20\text{ dBZ}$ ) to be included and avoid spurious convective core designations.

In Figure 11, we provide example cross sections through one of the idealized MCS events during its mature phase. The upper panels plot the cross sections for the vertical air velocity and the estimated reflectivity factor field as associated with the 1 km simulations (transect as from Figure 11e). The middle panels plot

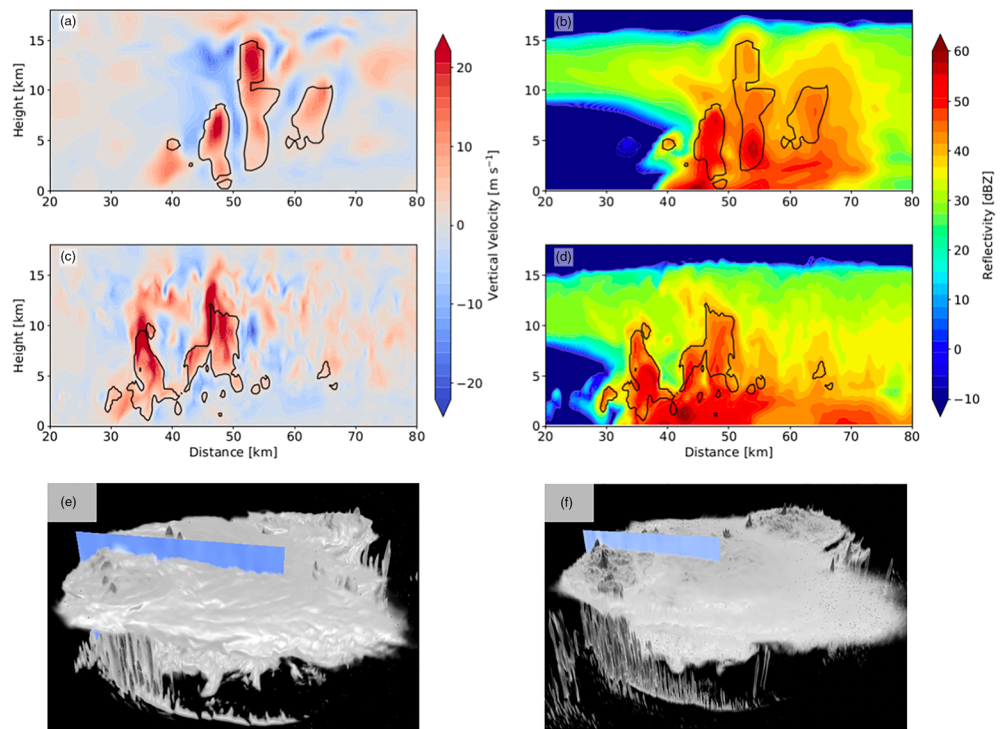


**Figure 11.** Cross sections through a mature idealized MCS simulation (a–d) with 1 km (a and b) and 250 m (c and d) grid spacings. Colored contours show vertical wind speed (a and c) and reflectivity (b and d), and black contours show identified updraft cores. A 3-D visualization of the cloud fields of the 1 km and 250 m simulations and the locations of the cross sections are shown in (e) and (f), respectively.

simulated results from the 250 m grid spacing run at the same time in the idealized simulation (Figure 11f). The cross section panels in Figures 11a–11d overlay the associated updraft “core” designations (black lines) as according to the velocity and reflectivity thresholds outlined above (e.g., 1 km or larger model grid scale objects within convective regions having  $|W| > 1.5$  m/s).

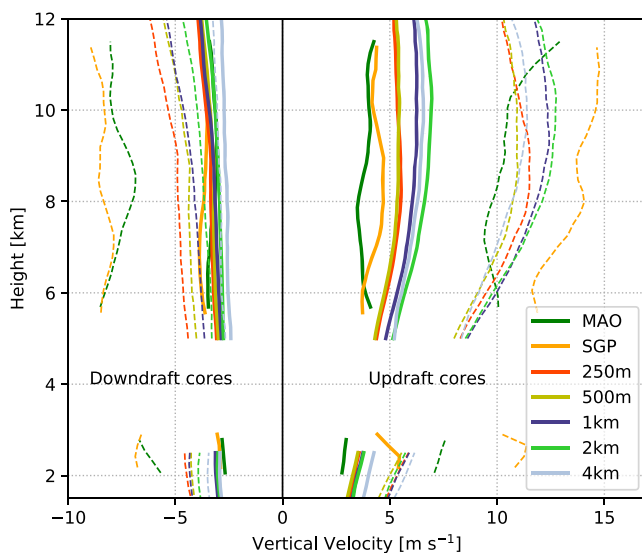


**Figure 12.** As in Figure 4b, but for convective cores within squall line locations having  $|W| > 1.5$  m/s for the WRF simulations with different horizontal grid spacings ( $\Delta x$  from 250 m to 4 km). The solid lines are the mean profiles, and the dashed lines are the 95th percentile profiles.

#### 4.2. Results of Model Observation Core Comparisons: Profile and PDF Properties

In Figure 12, we plot average core profiles as similar to previous examples in Figure 9. Mean updraft magnitudes from the simulations overestimate the mean observational retrieved profile behaviors as sampled at SGP and MAO. Since we are performing a similar form of random core sampling, these comparisons should both reflect similar expectation core  $\langle W \rangle$  under sampling bias. Moreover, we note that the model sampled 95th percentile updraft performances only slightly underestimate those from the SGP RWP observations, to be discussed below.

Figure 12 suggests that the more optimal updraft performances are those associated with the higher model resolutions (e.g., 250 and 500 m). Core results at these scales exhibit mean updraft profile behaviors closer (e.g., weaker) to the observations. This result accompanies the results that most model 95th percentile behaviors that reside in between the SGP and MAO observational extremes. In contrast to updraft properties, model downdrafts are underestimated at all model grid spacings when compared to the statistical RWP observations. Nevertheless, downdrafts are found to increase in intensity with increasing model resolution; thus, velocities

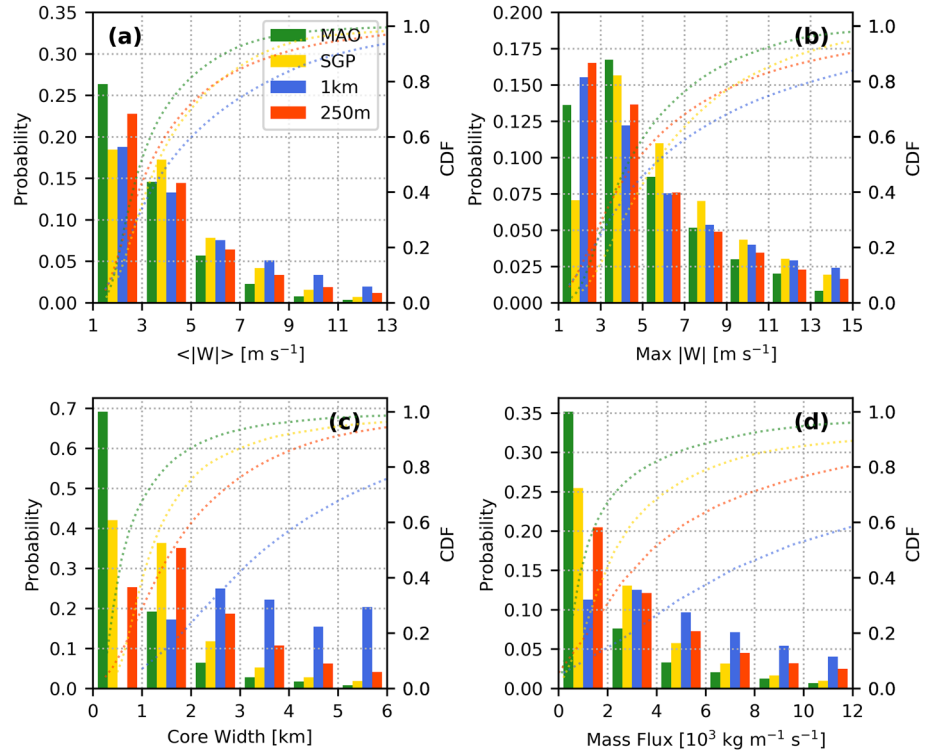


**Figure 13.** As in Figure 5 but for both observations (MAO and SGP) and WRF simulations with different horizontal grid spacings ( $\Delta x = 1$  km and 250 m).

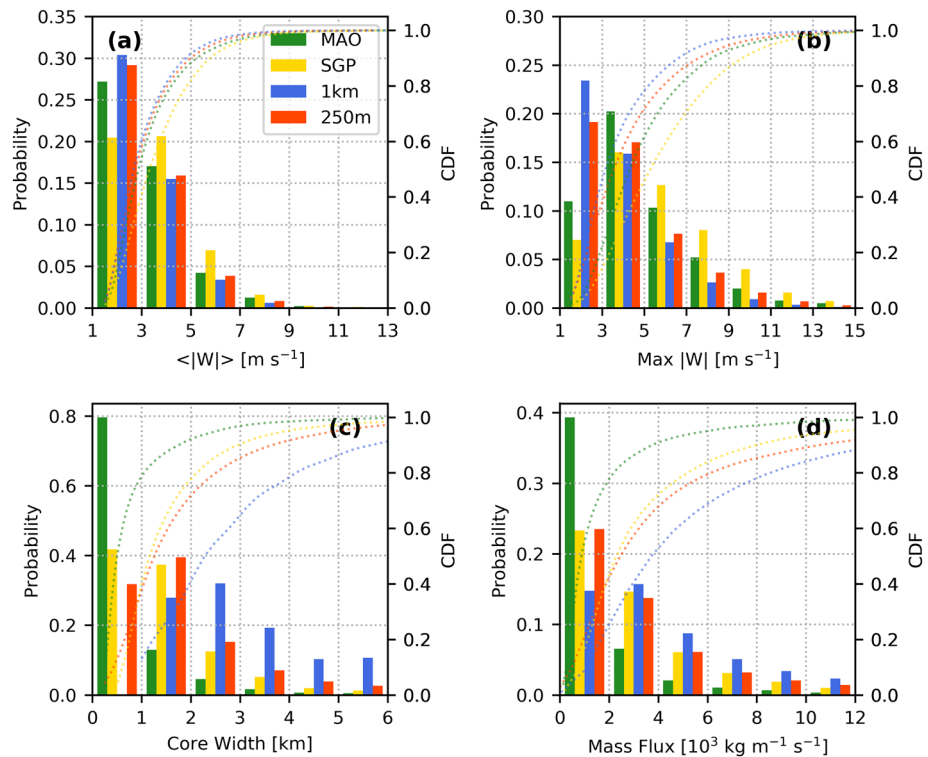


**Figure 14.** As in Figure 13 but for downdraft cores.



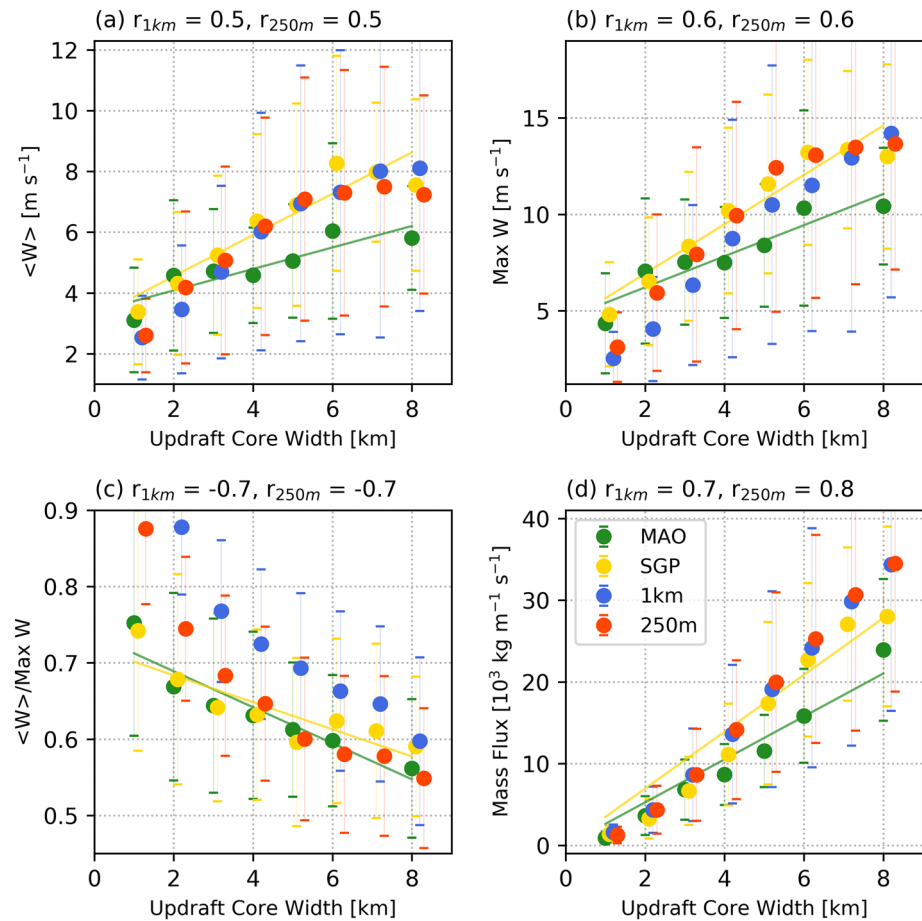


**Figure 15.** As in Figure 7 but for both observations (MAO and SGP) and WRF simulations with different horizontal grid spacings ( $\Delta x = 1$  km and 250 m).

sampled from the 250 m simulations are in better agreement with the observations. Again, one caveat of such comparisons between RWP observations and idealized model simulations is that they are statistical in nature, with the assumption that sampling in observations over many MCS events at one location is equivalent to sampling in simulations over a large area from a few idealized MCS events. Thus, we cannot rule out the possibility that differences between observations and simulations as in Figure 12 could arise from the differences in the thermodynamic environments (e.g., Table S3).

In Figure 13 (updrafts) and Figure 14 (downdrafts), we compare the 1-D histograms of core properties between the highest resolution 250 m runs, a standard 1 km grid spacing benchmark, and the observations. For completeness, we provide additional waterfall plots for the changes to these 1-D histograms (core width and mean core velocity retrievals) as a function of height for various model grid spacings compared to the SGP/MAO observations in our supplemental images (Figures S1–S4). The distributions from the 250 m simulations show an overall improvement compared to our SGP observations and the core properties at coarser model scales. In particular, simulated 250 m model updrafts align with a similar peak in the most frequently observed core mean/max value. However, cumulative displays of updraft magnitudes at all model resolutions skew toward more intense air motions (Figures 13a and 13b). We find the opposite behavior for downdraft cores, wherein most simulations are more frequently predicting smaller draft magnitudes and skew toward weaker intensities overall (Figures 14a and 14b). Coarser resolution model drafts indicate significantly higher frequencies for wider cores (updrafts and downdrafts) than we observe. Core widths in 250 m simulations are improved, indicating a similar size for the most frequently identified draft width. Since MCS simulations at all scales favor additional intense and larger cores, mass flux values also skew toward higher values than the observations. Not surprisingly, better model updraft and downdraft mass flux performances link to the coupled draft intensity and width improvements at the finer model grid spacings.

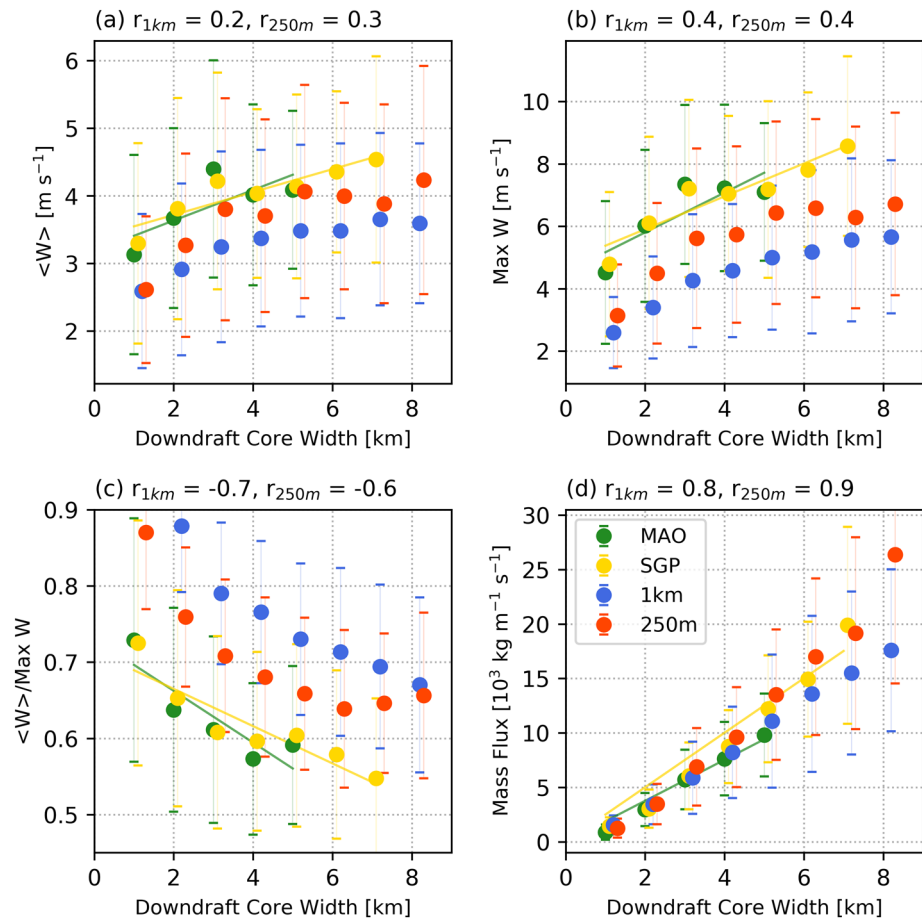


**Figure 16.** As in Figure 15 but for downdraft cores.

#### 4.3. Results of Model Observation Core Comparisons: 2-D Core Properties

We plot the 2-D core properties and size-intensity relationships between the simulations and observations in Figures 15 and 16. As consistent with the results in the above section, higher-resolution model properties compare the most favorably with the RWP observations. The model observational agreement is reasonable for the sampled range of RWP core widths with respect to updraft properties. Updraft cores at both 1 km and 250 m grid spacings align with observed mean/max performances for size-intensity relationships (Figure 15). Modeled updraft mass flux skews slightly larger than our observations at larger core sizes, but mean air motions are similar. Downdraft properties better converge to the observations for our 250 m simulations. Although updrafts are comparable at various model scales according to size-intensity depictions, the improvement in downdraft properties at finer grid scales is pronounced. For example, 250 m resolution simulations demonstrate an improvement in  $\langle W \rangle / W_{max}$  performance that also indicates a similar size dependence (negative correlation) as in the observations (e.g., Figure 15c). While there are similarities between the 1 km and 250 m simulation performances that suggest similar  $\langle W \rangle$ ,  $W_{max}$ , and mass flux trends for similarly sized updrafts, the shape parameter improvement suggests 250 m simulations are better at capturing the individual cores.

### 5. Discussion

It is difficult to compare RWP results with previous observational studies including aircraft observations that are typically drawn from limited cloud/event sampling, or core populations drawn from different cloud types and lifecycle stages. It is not surprising that we observe the most agreement to previous Oklahoma core studies that share similar instrument sampling, storm types, and record length. Overall, 1-D draft velocity distributions skew slightly weaker and smaller than those reported by Giangrande et al. (2013). This may be partially attributed to natural (event) variability and convective cloud types, as the Giangrande et al. (2013)

study included supercell thunderstorm overpasses that are typically attributed to having more intense, wider drafts. We note that the most frequently reported core size in Giangrande et al. (2013) was in the 1.5–2 km size bin, as compared to the peak found within the 1–1.5 km range for the current study. It is consistent that observations for weaker updrafts would also be those associated with smaller drafts. Since the most intense and widest cores we designate are also observed at the higher altitudes, such one-dimensional depictions are also influenced by conditional sampling biases (e.g., fewer but potentially fortuitous sampling aloft in mature or deeper convective events). Because of this, we did not prioritize such observations for subsequent model comparisons. Nevertheless, we note that core profile median/90/95th percentile properties with altitude (e.g., Figure 9) are similar in magnitude at similar altitudes to those found in Giangrande et al. (2013), their Figure 6. This also suggests that some 1-D profile differences between the two Oklahoma studies are due to differences in the lower-level core sampling and aggregation of such properties. This includes choices in our current study to avoid melting layer regions (between 3 and 5 km) that may be associated with a substantial number of smaller-sized cores with an absence of larger cores.

When considering model observational comparisons sharing similar forms of sampling limitations, our initial statistical investigations of the 250 m model grid spacing are nevertheless encouraging for the range of core widths observed by RWP and when considering the idealized setup of these simulations. For 250 m simulations, the model favors weaker and smaller updraft cores, corresponding also to higher core counts. These results are consistent with previous squall line modeling studies (e.g., Lebo & Morrison, 2015), here with RWP statistical observations supportive of this change in model performance. Although simulations and our observations suggest increasing core velocity magnitude (widening of distribution tails for updrafts/downdrafts) with altitude, the observations and finer grid-spacing model runs are less supportive for as pronounced an increase in core width with altitude to accompany this increase in core intensity. However, some model observation discrepancies may also be expected owing to our retrieval assumptions, such as assuming a constant storm motion with altitude.

One lingering criticism from these idealized simulation comparisons is the model tendency to simulate unrealistic large (in size) updraft cores (again, as in following our particular definitions) that may disproportionately influence mean air motion by a factor of 2 as was similarly reported in previous studies (e.g., Varble et al., 2014). However, our idealized simulations do not seem to indicate a poor performance in the 95th percentile profiles (as a proxy for maximum updrafts), or when looking at core populations for a given size bin. Here, we caution that this favorable performance may reflect a different limitation of our sampling, placing too much emphasis on the most extreme or less sampled conditions. Similarly, profile comparisons as in Figure 12 do not communicate the areal coverage occupied by updrafts/downdrafts, and favorable results do not exclude other deficiencies in mass flux characteristics. Note that since the model drafts tend to be less triangular than radar-designated drafts when not properly resolved, combined sampling biases (section 2.5) may argue that the models still encourage overestimation of maximum draft intensities as compared to similar observational sampling to coarser resolutions.

Overall, although size distributions of updraft cores improve at finer grid scales (e.g., Figure 13c and supplemental waterfall images Figures S1–S4), our performances help demonstrate the complex nature when communicating deficiencies in modeled updraft behaviors. Although many factors may contribute to these discrepancies, the frequency with which we designate additional intermediate to wider model core sizes (sizes between 4 and 8 km) is generally not consistent with our current observations (Figures 13a and 13b; supplemental plots). Moreover, models produce more frequent intense wide updraft cores with strong vertical velocities compared to RWP. Once again, for the updraft widths that the RWP most frequently designates applying our retrieval methods (core width <8 km), mean model 2-D size-intensity-mass flux relationships still appear quite reasonable for a given core width interval (e.g., Figure 15).

Moreover, within the typical range of core widths that the RWP observes, it is encouraging that these results indicate several bulk core relationships such as mass flux and velocities can already be realistically captured by kilometer-scale models. The biggest improvement we highlight is with the more realistic capture of convective downdraft properties at finer grid scales. Furthermore, updraft (core width) and downdraft (core width and intensity) improvements at finer grid scales are coupled, since an absence of convective downdrafts in coarser grid-scale simulations should be expected given coarser model inability to resolve strong horizontal gradients of vertical air motion and the (typically) more intense convective core updrafts mixing/dissipating downdrafts.

### Acknowledgments

This study was supported by the U.S. Department of Energy (DOE) Atmospheric System Research (ASR) Program and the Climate Model Development and Validation program. This paper has been authored by employees of Brookhaven Science Associates, LLC, under Contract DE-SC0012704 with the U.S. DOE. The publisher by accepting the paper for publication acknowledges that the U.S. Government retains a nonexclusive, paid-up, irrevocable, worldwide license to publish or reproduce the published form of this paper or allow others to do so, for U.S. Government purposes. The Pacific Northwest National Laboratory (PNNL) is operated for the DOE by Battelle Memorial Institute under Contract DE-AC06-76RLO1830. We also acknowledge the Atmospheric Radiation Measurement (ARM) program, a user facility of the U.S. DOE, Office of Science, sponsored by the Office of Biological and Environmental Research, and support from the ASR program of that office. This includes RWP mentors P. Muradyan and R. Coulter of Argonne National Laboratory for data collection and additional assistance. The National Center for Atmospheric Science (NCAR) is sponsored by the National Science Foundation (NSF), and this research was funded by NCAR's Hydrometeorological Applications Program. Dr. Prein is supported by DOE ASR Grant No. DE-SC0020050. We would like to acknowledge high-performance computing support from Cheyenne (doi:10.5065/D6RX99HX) provided by NCAR's Computational and Information Systems Laboratory, sponsored by the NSF. Similarly, we would wish to thank H. Morrison of NCAR for the discussion on model core behaviors and A. Varble and W. Gustafson of PNNL for internal reviews of this manuscript. We would like to thank the reviewers for their thoughtful and detailed comments. All ARM data sets used for this study can be downloaded at <https://www.arm.gov> and associated with several "value-added product" streams (Radar wind profiler data sets: <https://adc.arm.gov/discovery/#v/results/s/fsite::mao.M/finst::rwp>; Radiosonde data sets: <https://adc.arm.gov/discovery/#v/results/s/finst::sonde/fsite::sgp.P/fsite::mao.M/fac::sgp.C1/fac::mao.M1>; Disdrometer data sets: <https://adc.arm.gov/discovery/#v/results/s/finst::ldis/fsite::sgp.P/fsite::mao.M/fdpl::sgpldC1.b1/fdpl::maoldS10.b1>). The idealized MCS simulations will be available via ARM's archives.

## 6. Summary

This study documents deep convective updraft and downdraft characteristics using an extended RWP record at two locations (i.e., midlatitude continental U.S. and tropical central Amazon). The emphasis is on improving our understanding of convective cloud updraft and downdraft core properties including core width, shape, and intensity relationships. Our focus on mature-stage MCSs was done to help improve updraft and downdraft representativeness by mitigating one known limitation of previous aircraft/radar composite studies that aggregate different convection types (e.g., MCS and isolated cell) and lifecycle stages.

Further, we examine the usefulness of statistical RWP-retrieved core characteristics with an introductory model observational intercomparison of convective core properties. These efforts benefit from idealized WRF MCS simulations at various model grid spacings from 4 km to 250 m. Comparisons are performed in a manner that promotes similar 1-D and 2-D properties, including potential for biases therein (e.g., "chord-ing" type or convective line classification considerations applied to model and observations as consistently as was possible given model output resolution). We find that improving the model grid spacing down to 250 m scales helps MCS simulations better resolve statistical updraft and downdraft magnitudes, core width, and profile details. We suggest significant model improvement in convective downdraft representations (width, intensity, and shape) to accompany improvements in updraft behaviors (width and shape).

Three key results of this study are as follows:

1. Mature-stage MCS core properties share similar characteristics to the findings of previous aircraft and radar-based studies. This includes behaviors such as (a) estimated vertical air motions (core updrafts and downdrafts) increasing with altitude; (b) extremes in updraft and downdraft air motions exceeding 10 m/s to the higher altitudes; (c) positive correlations ( $r \sim 0.4$ – $0.5$ ) between draft size and intensity; and (d) similar 2-D core mass flux values.
2. Amazon core properties align with previous maritime tropical convective examples (e.g., May & Rajopadhyaya, 1996), whereas Oklahoma MCS core characteristics and statistical profiles are comparable, with 1-D core properties skewed slightly smaller/weaker than previous Oklahoma efforts that included supercell thunderstorms (e.g., Giangrande et al., 2013). The MCS draft properties from the Oklahoma MCSs are significantly more intense, larger, and having enhanced draft mass flux (for a similarly sized core) than the observations from mature-phase Amazon MCSs. These findings are consistent with larger-scale forcing for Oklahoma events and steeper ELRs, despite Amazon events favoring similar or larger CAPE and CIN values (e.g., "skinny" or "fatter" CAPE arguments as in Lucas et al., 1994a, 1994b). Downdrafts are also more intense and more frequent to higher altitudes for the Oklahoma events than Amazon MCSs, as consistent with Wang et al. (2019) and physical arguments therein. Interestingly, Amazon MCS properties do not vary significantly between wet to dry season examples, suggesting seasonal variability in MCS conditions is not as important to these properties as perhaps with widespread or isolated convective regimes (e.g., Giangrande et al., 2016).
3. A model observational intercomparison for statistical draft properties is performed using idealized WRF simulations consistent with the midlatitude continental (SGP) MCS environments. It is shown that the model simulations performed at  $\Delta x = 250$  m for mature MCS stages were also those that exhibit improved convective core draft intensity, mass flux, width, and shape parameter performances. These performances were more consistent between the midlatitude observations and idealized model forcing conditions. Although all simulations predict more frequent intermediate to larger-sized updraft cores, the results indicate that core mass flux, air motions, and size relationships can be realistically captured by kilometer scale models within the ranges of core sizes the RWP typically retrieves (widths < 8 km). The most pronounced improvement we observe was the more realistic downdraft treatments at finer model resolutions.

## References

- ARM (2014). Laser disdrometer (PARS2). 2014-01-01 to 2015-11-30, Arm Mobile Facility (MAO) Manacapuru, Amazonas, Brazil; AMF1 (m1); 2012-01-01 to 2016-12-31, Southern Great Plains (SGP) central facility, Lamont, OK (C1). ARM Data Center. Retrieved from <http://doi.org/10.5439/1150252> (Compiled by M. Bartholomew, Y. Shi and D. Wang. Data set accessed 2019-01-20.) <https://doi.org/10.5439/1150252>
- ARM (2019). Balloon-Borne Sounding System (SONDEWPN). 2014-01-01 to 2015-11-30, Arm Mobile Facility (MAO) Manacapuru, Amazonas, Brazil; AMF1 (m1); 2012-01-01 to 2016-12-31, Southern Great Plains (SGP) central facility, Lamont, OK (C1). ARM Data Center. Retrieved from <http://doi.org/10.5439/1021460> (Compiled by D. Holdridge, R. Coulter, D. Holdridge, M. Ritsche, R. Coulter, J. Kyrouac and E. Keeler. Data set accessed 2019-01-20.) <https://doi.org/10.5439/1021460>



- Anderson, N. F., Grainger, C. A., & Stith, J. L. (2005). Characteristics of strong updrafts in precipitation systems over the central tropical Pacific Ocean and in the Amazon. *Journal of Applied Meteorology*, 44(5), 731–738. <https://doi.org/10.1175/JAM2231.1>
- Bryan, G. H., & Morrison, H. (2012). Sensitivity of a simulated squall line to horizontal resolution and parameterization of microphysics. *Monthly Weather Review*, 140(1), 202–225. <https://doi.org/10.1175/MWR-D-11-00046.1>
- Bryan, G. H., Wyngaard, J. C., & Fritsch, J. M. (2003). Resolution requirements for the simulation of deep moist convection. *Monthly Weather Review*, 131(10), 2394–2416. [https://doi.org/10.1175/1520-0493\(2003\)131<2394:RRFTSO>2.0.CO;2](https://doi.org/10.1175/1520-0493(2003)131<2394:RRFTSO>2.0.CO;2)
- Byers, H. R., & Braham, R. R. (1948). Thunderstorm structure and circulation. *Journal of Meteorology*, 5(3), 71–86. [https://doi.org/10.1175/1520-0469\(1948\)005<0071:TSAC>2.0.CO;2](https://doi.org/10.1175/1520-0469(1948)005<0071:TSAC>2.0.CO;2)
- Dee, D. P., Uppala, S. M., Simmons, A. J., Berrisford, P., Poli, P., Kobayashi, S., et al. (2011). The ERA-Interim reanalysis: Configuration and performance of the data assimilation system. *Quarterly Journal of the Royal Meteorological Society*, 137(656), 553–597. <https://doi.org/10.1002/qj.828>
- Del Genio, A. D., & Kovari, W. (2002). Climatic properties of tropical precipitating convection under varying environmental conditions. *Journal of Climate*, 15(18), 2597–2615. [https://doi.org/10.1175/1520-0442\(2002\)015<2597:CPOTPC>2.0.CO;2](https://doi.org/10.1175/1520-0442(2002)015<2597:CPOTPC>2.0.CO;2)
- Del Genio, A. D., Wu, J., & Chen, Y. (2012). Characteristics of mesoscale organization in WRF simulations of convection during TWP-ICE. *Journal of Climate*, 25(17), 5666–5688. <https://doi.org/10.1175/JCLI-D-11-00422.1>
- Diffenbaugh, N. S., Scherer, M., & Trapp, R. J. (2013). Robust increases in severe thunderstorm environments in response to greenhouse forcing. *Proceedings of the National Academy of Sciences*, 110(41), 16,361–16,366. <https://doi.org/10.1073/pnas.1307758110>
- Donner, L. J., O'Brien, T. A., Rieger, D., Vogel, B., & Cooke, W. F. (2016). Are atmospheric updrafts a key to unlocking climate forcing and sensitivity? *Atmospheric Chemistry and Physics*, 16(20), 12,983–12,992. <https://doi.org/10.5194/acp-16-12983-2016>
- Fabry, F., & Zawadzki, I. (1995). Long-term radar observations of the melting layer of precipitation and their interpretation. *Journal of the Atmospheric Sciences*, 52(7), 838–851. [https://doi.org/10.1175/1520-0469\(1995\)052<0838:LTRoot>2.0.CO;2](https://doi.org/10.1175/1520-0469(1995)052<0838:LTRoot>2.0.CO;2)
- Fan, J., Han, B., Varble, A., Morrison, H., North, K., Kollias, P., et al. (2017). Cloud-resolving model intercomparison of an MC3E squall line case: Part I—Convective updrafts. *Journal of Geophysical Research: Atmospheres*, 122, 9351–9378. <https://doi.org/10.1002/2017JD026622>
- Feng, Z., Dong, X., Xi, B., McFarlane, S. A., Kennedy, A., Lin, B., & Minnis, P. (2012). Life cycle of midlatitude deep convective systems in a Lagrangian framework. *Journal of Geophysical Research*, 117, D23201. <https://doi.org/10.1029/2012JD018362>
- Feng, Z., & Giangrande, S. (2018). Merged RWP-WACR-ARSCL cloud mask and cloud type. <https://doi.org/10.5439/1462693>
- Feng, Z., Houze, R. A., Leung, L. R., Song, F., Hardin, J. C., Wang, J., et al. (2019). Spatiotemporal characteristics and large-scale environments of mesoscale convective systems east of the rocky mountains. *Journal of Climate*, 32(21), 7303–7328. <https://doi.org/10.1175/JCLI-D-19-0137.1>
- Feng, Z., Leung, L. R., Hagos, S., Houze, R. A., Burleyson, C. D., & Balaguru, K. (2016). More frequent intense and long-lived storms dominate the springtime trend in central US rainfall. *Nature of Communication*, 7, 13429. <https://doi.org/10.1038/ncomms13429>
- Feng, Z., Leung, L. R., Houze, R. A., Hagos, S., Hardin, J., Yang, Q., et al. (2018). Structure and evolution of mesoscale convective systems: Sensitivity to cloud microphysics in convection-permitting simulations over the united states. *Journal of Advances in Modeling Earth Systems*, 10, 1470–1494. <https://doi.org/10.1029/2018MS001305>
- Fritsch, J. M., Kane, R. J., & Chelius, C. R. (1986). The contribution of mesoscale convective weather systems to the warm-season precipitation in the united states. *Journal of Climate and Applied Meteorology*, 25(10), 1333–1345. [https://doi.org/10.1175/1520-0450\(1986\)025<1333:TCOMCW>2.0.CO;2](https://doi.org/10.1175/1520-0450(1986)025<1333:TCOMCW>2.0.CO;2)
- Geerts, B., & Dawei, Y. (2004). Classification and characterization of tropical precipitation based on high-resolution airborne vertical incidence radar. Part I: Classification. *Journal of Applied Meteorology (1988-2005)*, 43(11), 1554–1566. Retrieved from <http://www.jstor.org/stable/26186013>
- Giangrande, S. E., Collis, S., Straka, J., Protat, A., Williams, C., & Krueger, S. (2013). A summary of convective-core vertical velocity properties using ARM UHF wind profilers in Oklahoma. *Journal of Applied Meteorology and Climatology*, 52(10), 2278–2295. <https://doi.org/10.5194/acp-17-14519-2017>
- Giangrande, S. E., Feng, Z., Jensen, M. P., Comstock, J. M., Johnson, K. L., Toto, T., et al. (2017). Cloud characteristics, thermodynamic controls and radiative impacts during the observations and modeling of the Green Ocean Amazon (GoAmazon2014/5) experiment. *Atmospheric Chemistry and Physics*, 17(23), 14,519–14,541. <https://doi.org/10.5194/acp-17-14519-2017>
- Giangrande, S. E., Toto, T., Jensen, M. P., Bartholomew, M. J., Feng, Z., Protat, A., et al. (2016). Convective cloud vertical velocity and mass-flux characteristics from radar wind profiler observations during GoAmazon2014/5. *Journal of Geophysical Research: Atmospheres*, 121, 12,891–12,913. <https://doi.org/10.1002/2016JD025303>
- Hartmann, D. L., Hendon, H. H., & Houze, R. A. (1984). Some implications of the mesoscale circulations in tropical cloud clusters for large-scale dynamics and climate. *Journal of the Atmospheric Sciences*, 41(1), 113–121. [https://doi.org/10.1175/1520-0469\(1984\)041<0113:SIOTMC>2.0.CO;2](https://doi.org/10.1175/1520-0469(1984)041<0113:SIOTMC>2.0.CO;2)
- Heymsfield, G. M., Tian, L., Heymsfield, A. J., Li, L., & Guimond, S. (2010). Characteristics of deep tropical and subtropical convection from nadir-viewing high-altitude airborne Doppler radar. *Journal of the Atmospheric Sciences*, 67(2), 285–308. <https://doi.org/10.1175/2009JAS3132.1>
- Houze, R. A. (2004). Mesoscale convective systems. *Reviews of Geophysics*, 42, RG4003. <https://doi.org/10.1029/2004RG000150>
- Houze, R. A. Jr. (2018). 100 years of research on mesoscale convective systems. *Meteorological Monographs*, 59, 17.1–17.54. <https://doi.org/10.1175/AMSMONOGRAPH-D-18-0001.1>
- Hu, X.-M., Klein, P. M., & Xue, M. (2013). Evaluation of the updated YSU planetary boundary layer scheme within WRF for wind resource and air quality assessments. *Journal of Geophysical Research: Atmospheres*, 118, 10,490–10,505. <https://doi.org/10.1002/jgrd.50823>
- Janjic, Z. I. (2002). Nonsingular implementation of the Mellor-Yamada level 2.5 scheme in the NCEP Meso model. NCEP office Note 437, 61.
- Jorgensen, D. P., Zipser, E. J., & LeMone, M. A. (1985). Vertical motions in intense hurricanes. *Journal of the Atmospheric Sciences*, 42(8), 839–856.
- Kollias, P., Battaglia, A., Tatarevic, A., Lamer, K., Tridon, F., & Pfizenmaier, L. (2018). The earthcare cloud profiling radar (CPR) doppler measurements in deep convection: Challenges, post-processing, and science applications. In (Vol. 10776). Retrieved from <https://doi.org/10.1117/12.2324321>
- Kumar, V. V., Jakob, C., Protat, A., Williams, C. R., & May, P. T. (2015). Mass-flux characteristics of tropical cumulus clouds from wind profiler observations at Darwin, Australia. *Journal of the Atmospheric Sciences*, 72(5), 1837–1855. <https://doi.org/10.1175/JAS-D-14-0259.1>
- Kuo, H. L., & Raymond, W. H. (1980). A quasi-one-dimensional cumulus cloud model and parameterization of cumulus heating and mixing effects. *Monthly Weather Review*, 108(7), 991–1009. [https://doi.org/10.1175/1520-0493\(1980\)108<0991:AQODCC>2.0.CO;2](https://doi.org/10.1175/1520-0493(1980)108<0991:AQODCC>2.0.CO;2)
- LeMone, M. A., & Zipser, E. J. (1980). Cumulonimbus vertical velocity events in gate. Part I: Diameter, intensity and mass flux. *Journal of the Atmospheric Sciences*, 37(11), 2444–2457. [https://doi.org/10.1175/1520-0469\(1980\)037<2444:CVVEIG>2.0.CO;2](https://doi.org/10.1175/1520-0469(1980)037<2444:CVVEIG>2.0.CO;2)



- Lebo, Z. J., & Morrison, H. (2015). Effects of horizontal and vertical grid spacing on mixing in simulated squall lines and implications for convective strength and structure. *Monthly Weather Review*, 143(11), 4355–4375. <https://doi.org/10.1175/MWR-D-15-0154.1>
- Liu, C., Ikeda, K., Rasmussen, R., Barlage, M., Newman, A. J., Prein, A. F., et al. (2017). Continental-scale convection-permitting modeling of the current and future climate of North America. *Climate Dynamics*, 49, 71–95.
- Lucas, C., Zipser, E. J., & LeMone, M. A. (1994a). Convective available potential energy in the environment of oceanic and continental clouds: Correction and comments. *Journal of the Atmospheric Sciences*, 51(24), 3829–3830. [https://doi.org/10.1175/1520-0469\(1994\)051<3829:CAPEIT>2.0.CO;2](https://doi.org/10.1175/1520-0469(1994)051<3829:CAPEIT>2.0.CO;2)
- Lucas, C., Zipser, E. J., & LeMone, M. A. (1994b). Vertical velocity in oceanic convection off tropical Australia. *Journal of the Atmospheric Sciences*, 51(21), 3183–3193. [https://doi.org/10.1175/1520-0469\(1994\)051<3183:VVIOCO>2.0.CO;2](https://doi.org/10.1175/1520-0469(1994)051<3183:VVIOCO>2.0.CO;2)
- Martin, S. T., Artaxo, P., Machado, L. A. T., Manzi, A. O., Souza, R. A. F., Schumacher, C., et al. (2016). Introduction: Observations and modeling of the Green Ocean Amazon (GoAmazon2014/5). *Atmospheric Chemistry and Physics*, 16(8), 4785–4797. <https://doi.org/10.5194/acp-16-4785-2016>
- Martin, S. T., Artaxo, P., Machado, L., Manzi, A. O., Souza, R. A. F., Schumacher, C., et al. (2017). The Green Ocean Amazon experiment (GoAmazon2014/5) observes pollution affecting gases, aerosols, clouds, and rainfall over the rain forest. *Bulletin of the American Meteorological Society*, 98(5), 981–997. <https://doi.org/10.1175/BAMS-D-15-00221.1>
- Mather, J. H., & Voiles, J. W. (2013). The arm climate research facility: A review of structure and capabilities. *Bulletin of the American Meteorological Society*, 94(3), 377–392. <https://doi.org/10.1175/BAMS-D-11-00218.1>
- May, P. T., & Rajopadhyaya, D. K. (1996). Wind profiler observations of vertical motion and precipitation microphysics of a tropical squall line. *Monthly Weather Review*, 124(4), 621–633. [https://doi.org/10.1175/1520-0493\(1996\)124<0621:WPOOVM>2.0.CO;2](https://doi.org/10.1175/1520-0493(1996)124<0621:WPOOVM>2.0.CO;2)
- May, P. T., & Rajopadhyaya, D. K. (1999). Vertical velocity characteristics of deep convection over Darwin, Australia. *Monthly Weather Review*, 127(6), 1056–1071.
- Miller, M. A., Nitschke, K., Ackerman, T. P., Ferrell, W., Hickmon, N., & Ivey, M. (2016). The atmospheric radiation measurement mobile facility, the atmospheric radiation measurement (ARM) program: the first 20 years of ARM. *Meteorological Monographs*, 57, 9.1–9.15.
- Morrison, H. (2016). Impacts of updraft size and dimensionality on the perturbation pressure and vertical velocity in cumulus convection. Part I: Simple, generalized analytic solutions. *Journal of the Atmospheric Sciences*, 73(4), 1441–1454. <https://doi.org/10.1175/JAS-D-15-0040.1>
- Morrison, H. (2017). An analytic description of the structure and evolution of growing deep cumulus updrafts. *Journal of the Atmospheric Sciences*, 74(3), 809–834. <https://doi.org/10.1175/JAS-D-16-0234.1>
- Mrowiec, A. A., Rio, C., Fridlind, A. M., Ackerman, A. S., Del Genio, A. D., Pauluis, O. M., et al. (2012). Analysis of cloud-resolving simulations of a tropical mesoscale convective system observed during TWP-ICE: Vertical fluxes and draft properties in convective and stratiform regions. *Journal of Geophysical Research*, 117, D19201. <https://doi.org/10.1029/2012JD017759>
- Nesbitt, S. W., Cifelli, R., & Rutledge, S. A. (2006). Storm morphology and rainfall characteristics of TRMM precipitation features. *Monthly Weather Review*, 134(10), 2702–2721. <https://doi.org/10.1175/MWR3200.1>
- North, K. W., Oue, M., Kollias, P., Giangrande, S. E., Collis, S. M., & Potvin, C. K. (2017). Vertical air motion retrievals in deep convective clouds using the ARM scanning radar network in Oklahoma during MC3E. *Atmospheric Measurement Techniques*, 10(8), 2785–2806. <https://doi.org/10.5194/amt-10-2785-2017>
- Oue, M., Kollias, P., Shapiro, A., Tatarevic, A., & Matsui, T. (2019). Investigation of observational error sources in multi-Doppler-radar three-dimensional variational vertical air motion retrievals. *Atmospheric Measurement Techniques*, 12(3), 1999–2018. <https://doi.org/10.5194/amt-12-1999-2019>
- Ovchinnikov, M., Giangrande, S., Larson, V. E., Protat, A., & Williams, C. R. (2019). Dependence of vertical alignment of cloud and precipitation properties on their effective fall speeds. *Journal of Geophysical Research: Atmospheres*, 124, 2079–2093. <https://doi.org/10.1029/2018JD029346>
- Powers, J. G., Klemp, J. B., Skamarock, W. C., Davis, C. A., Dudhia, J., Gill, D. O., et al. (2017). The weather research and forecasting model: Overview, system efforts, and future directions. *Bulletin of the American Meteorological Society*, 98(8), 1717–1737. <https://doi.org/10.1175/BAMS-D-15-00308.1>
- Prein, A. F., Liu, C., Ikeda, K., Bullock, R., Rasmussen, R. M., Holland, G. J., & Clark, M. (2017). Simulating North American mesoscale convective systems with a convection-permitting climate model. *Climate Dynamics*. <https://doi.org/10.1007/s00382-017-3993-2>
- Ray, P. S., Ziegler, C. L., Bumgarner, W., & Serafin, R. J. (1980). Single- and multiple-Doppler radar observations of tornadic storms. *Monthly Weather Review*, 108(10), 1607–1625. [https://doi.org/10.1175/1520-0493\(1980\)108<1607:SAMDRO>2.0.CO;2](https://doi.org/10.1175/1520-0493(1980)108<1607:SAMDRO>2.0.CO;2)
- Roca, R., Aublanc, J., Chambon, P., Fiolleau, T., & Viltard, N. (2014). Robust observational quantification of the contribution of mesoscale convective systems to rainfall in the tropics. *Journal of Climate*, 27(13), 4952–4958. <https://doi.org/10.1175/JCLI-D-13-00628.1>
- Seeley, J. T., & Roms, D. M. (2015). The effect of global warming on severe thunderstorms in the United States. *Journal of Climate*, 28(6), 2443–2458. <https://doi.org/10.1175/JCLI-D-14-00382.1>
- Sillmann, J., Kharin, V. V., Zhang, X., Zwiers, F. W., & Bronaugh, D. (2013). Climate extremes indices in the CMIP5 multimodel ensemble: Part 1. Model evaluation in the present climate. *Journal of Geophysical Research: Atmospheres*, 118, 1716–1733. <https://doi.org/10.1002/jgrd.50203>
- Sisterson, D. L., Peppler, R. A., Cress, T. S., Lamb, P. J., & Turner, D. D. (2016). The ARM Southern Great Plains (SGP) site. *Meteorological Monographs*, 57, 6.1–6.14. <https://doi.org/10.1175/AMSMONOGRAPH-D-16-0004.1>
- Skamarock, W. C. (2004). Evaluating mesoscale NWP models using kinetic energy spectra. *Monthly Weather Review*, 132(12), 3019–3032. <https://doi.org/10.1175/MWR2830.1>
- Song, F., Feng, Z., Leung, L. R., Houze Jr, R. A., Wang, J., Hardin, J., & Homeyer, C. R. (2019). Contrasting spring and summer large-scale environments associated with mesoscale convective systems over the U.S. great plains. *Journal of Climate*, 32(20), 6749–6767. <https://doi.org/10.1175/JCLI-D-18-0839.1>
- Steiner, M., Houze, R. A., & Yuter, S. E. (1995). Climatological characterization of three-dimensional storm structure from operational radar and rain gauge data. *Journal of Applied Meteorology*, 34(9), 1978–2007. [https://doi.org/10.1175/1520-0450\(1995\)034<1978:CCOTDS>2.0.CO;2](https://doi.org/10.1175/1520-0450(1995)034<1978:CCOTDS>2.0.CO;2)
- Stith, J. L., Haggerty, J. A., Heymsfield, A., & Grainger, C. A. (2004). Microphysical characteristics of tropical updrafts in clean conditions. *Journal of Applied Meteorology*, 43(5), 779–794. <https://doi.org/10.1175/2104.1>
- Thompson, G., Field, P. R., Rasmussen, R. M., & Hall, W. D. (2008). Explicit forecasts of winter precipitation using an improved bulk microphysics scheme. Part II: Implementation of a new snow parameterization. *Monthly Weather Review*, 136(12), 5095–5115. <https://doi.org/10.1175/2008MWR2387.1>
- Trapp, R. J., Diefenbaugh, N. S., & Gluhovsky, A. (2009). Transient response of severe thunderstorm forcing to elevated greenhouse gas concentrations. *Geophysical Research Letters*, 36, L01703. <https://doi.org/10.1029/2008GL036203>

- Tridon, F., Battaglia, A., Kollias, P., Luke, E., & Williams, C. R. (2013). Signal postprocessing and reflectivity calibration of the atmospheric radiation measurement 915-MHz wind profilers. *Journal of Atmospheric and Oceanic Technology*, 30, 1038–1054.
- Varble, A., Zipser, E. J., Fridlind, A. M., Zhu, P., Ackerman, A. S., Chaboureaud, J.-P., et al. (2014). Evaluation of cloud-resolving and limited area model intercomparison simulations using TWP-ICE observations: 1. Deep convective updraft properties. *Journal of Geophysical Research: Atmospheres*, 119, 13,891–13,918. <https://doi.org/10.1002/2013JD021371>
- Wang, D., Giangrande, S. E., Schiro, K. A., Jensen, M. P., & Houze, R. A. Jr. (2019). The characteristics of tropical and midlatitude mesoscale convective systems as revealed by radar wind profilers. *Journal of Geophysical Research: Atmospheres*, 124, 4601–4619. <https://doi.org/10.1029/2018JD030087>
- Williams, C. R. (2012). Vertical air motion retrieved from dual-frequency profiler observations. *Journal of Atmospheric and Oceanic Technology*, 29(10), 1471–1480. <https://doi.org/10.1175/JTECH-D-11-00176.1>
- Williams, C. R., Ecklund, W. L., & Gage, K. S. (1995). Classification of precipitating clouds in the tropics using 915-MHz wind profilers. *Journal of Atmospheric and Oceanic Technology*, 12(5), 996–1012. [https://doi.org/10.1175/1520-0426\(1995\)012<0996:COPCIT>2.0.CO;2](https://doi.org/10.1175/1520-0426(1995)012<0996:COPCIT>2.0.CO;2)
- Wu, J., Del Genio, A. D., Yao, M.-S., & Wolf, A. B. (2009). Wrf and GISS SCM simulations of convective updraft properties during TWP-ICE. *Journal of Geophysical Research*, 114, D04206. <https://doi.org/10.1029/2008JD010851>
- Ziegler, C. L., Mansell, E. R., Straka, J. M., MacGorman, D. R., & Burgess, D. W. (2010). The impact of spatial variations of low-level stability on the life cycle of a simulated supercell storm. *Monthly Weather Review*, 138(5), 1738–1766. <https://doi.org/10.1175/2009MWR3010.1>
- Zipser, E. J. (1977). Mesoscale and convective-scale downdrafts as distinct components of squall-line structure. *Monthly Weather Review*, 105(12), 1568–1589. [https://doi.org/10.1175/1520-0493\(1977\)105<1568:MACDAD>2.0.CO;2](https://doi.org/10.1175/1520-0493(1977)105<1568:MACDAD>2.0.CO;2)
- Zipser, E. J., & LeMone, M. A. (1980). Cumulonimbus vertical velocity events in gate. Part II: Synthesis and model core structure. *Journal of the Atmospheric Sciences*, 37(11), 2458–2469. [https://doi.org/10.1175/1520-0469\(1980\)037<2458:CVVEIG>2.0.CO;2](https://doi.org/10.1175/1520-0469(1980)037<2458:CVVEIG>2.0.CO;2)